Nanoscale Advances

ROYAL SOCIETY OF CHEMISTRY

PAPER

View Article Online
View Journal | View Issue

Open Access Article. Published on 22 July 2025. Downloaded on 12/8/2025 6:04:23 AM.
This article is licensed under a Creative Commons Attribution-NonCommercial 3.0 Unported Licence.

Check for updates

Cite this: *Nanoscale Adv.*, 2025, **7**, 5681

Tuning the electrochemical performance of a hierarchical MoO_3/CdO binary heterostructure for supercapacitor applications†

Saifullah,[a] Probal Roy,[a] Md. Abdullah Zubair[b] and Muhammad Rakibul Islam*[a]

Cadmium oxide (CdO)-incorporating molybdenum trioxide (MoO_3) nanocomposites were synthesized using a facile hydrothermal method by varying the CdO content (1%, 3%, and 5%) to comprehend the influence of CdO concentration on the electrochemical performance of MoO_3. The structural and morphological properties of the synthesized nanomaterials were characterized using X-ray diffraction (XRD) and field emission scanning electron microscopy (FE-SEM). XRD showed that MoO_3 has an orthorhombic structure, and FE-SEM showed that it has a nanobelt shape (0.8–3.2 μm long and 100–228 nm wide) with CdO nanoparticles grown on its surface. Electrochemical properties were analyzed through cyclic voltammetry (CV), galvanostatic charge–discharge (GCD), and electrochemical impedance spectroscopy (EIS). The 3%CdO-incorporating MoO_3 electrode exhibited a higher specific capacitance of 671 F g^{-1} at a current density of 0.50 A g^{-1}, while the pristine MoO_3 shows 386 F g^{-1}. Kinetic analysis of CV data indicates that redox processes in the nanocomposite electrodes involve both capacitive and diffusion-controlled mechanisms. The MoO_3/CdO (3%) electrode showed low charge transfer resistance (2.35 Ω) and series resistance (6.20 Ω), enabling faster faradaic redox reactions and improved electrochemical performance. Moreover, the MoO_3/CdO (3%) electrode demonstrated excellent cycling stability, retaining more than 92% of its initial specific capacitance after 5000 cycles. The incorporation of CdO enhances the diffusion pathways within the nanocomposites, potentially boosting their conductivity and specific capacitance. The symmetric supercapacitor MoO_3/CdO (3%)//MoO_3/CdO (3%) exhibited a notable operating voltage of 1.6 V, achieving an energy density of 124 W h kg^{-1} at a power density of 1067 W kg^{-1}. It also exhibited a capacitance retention of 88.9% after 5000 cycles at a current density of 15 A g^{-1}, highlighting its potential for energy storage applications.

Received 18th May 2025
Accepted 19th July 2025

DOI: 10.1039/d5na00491h

rsc.li/nanoscale-advances

1. Introduction

Rapid global economic growth and industrialization have resulted in a severe energy crisis, creating significant societal challenges. The increasing global energy demand drives technological innovations in developing systems for storing and delivering clean, renewable energy.[1] To address this issue, scientists have successfully developed new renewable energy sources that are now used daily, including solar, tidal, and wind energy.[2] However, the range of feasible applications is limited since these sources depend on local climate and geographical conditions.[3] As a result, there is a need for competent and environmentally friendly energy storage and conversion devices to store and conversion technologies that can reliably store and provide the required energy consistently and without disruption.[4] Electrochemical energy storage devices are unique among other energy storage and conversion technologies and have grown to be a vital renewable energy source in people's daily lives.[5,6] Fuel cells, supercapacitors (SCs), and several kinds of batteries are examples of electrochemical energy storage systems that store energy as a charge.[7] SCs are among the most promising energy storage devices, often called ultracapacitors or electrochemical capacitors. Their extended longevity, superior cycle stability, and quick charge–discharge rates allow them to fill the gap between batteries and traditional capacitors.[8–14] Still, their poor energy density is seen as a significant challenge in the search for effective energy storage technologies. Considerable attention has been focused on enhancing the energy density. Improving specific capacitance and expanding the potential window are key strategies to boost energy density (E), as E is directly proportional to capacitance (C) and the square of the potential window (V), according to $E = (1/2)CV^2$. Several strategies are employed to improve the specific capacitance and the overall performance of SC electrodes.[15] The progress of nanostructured electrode materials has been one of the exciting

[a]Department of Physics, Bangladesh University of Engineering and Technology, Dhaka, Bangladesh

[b]Department of Nanomaterials and Ceramic Engineering, Bangladesh University of Engineering and Technology, Dhaka, Bangladesh. E-mail: rakibul@phy.buet.ac.bd

† Electronic supplementary information (ESI) available. See DOI: https://doi.org/10.1039/d5na00491h

Open Access Article. Published on 22 July 2025. Downloaded on 12/8/2025 6:04:23 AM. This article is licensed under a Creative Commons Attribution-NonCommercial 3.0 Unported Licence.

strategies studied to overcome the low energy density of SCs. The high surface area, nanosize effects, and significantly enhanced kinetics make them more attractive for developing better SCs.[16–20] Electrode materials are an essential component of SCs and include carbon materials, metal oxides, metal nitrides, metal phosphides, metal hydroxides, metal carbides, conductive polymers, metal sulfides, and chalcogenides.[16,21] Transition metal oxides (TMOs) attract greater interest due to their several unique benefits, including increased capacity, energy density, and faster charge transfer dynamics.[13,22]

Many pseudocapacitive energy materials have been studied and found to have relatively high specific capacitance, including CeO_2,[23] Co_3O_4,[24] Fe_2O_3,[25] MnO_2,[26] MoO_3,[27] NiO,[28] RuO_2,[29] SnO_2,[30] TiO_2,[31] V_2O_5,[32] WO_3,[33] ZnO,[34] and so on. Among these, molybdenum trioxide (MoO_3) is a significant TMO. It is a promising alternative for the electrode in SCs due to its elevated potential window in neutral aqueous electrolytes, enhanced stability, as well as its higher theoretical capacity, cost-effectiveness, and fine electrochemical behavior.[35,36] MoO_3 outperforms the other TMOs due to its wide range of oxidation states and diverse crystallographic structures, including orthorhombic, hexagonal, and monoclinic.[37] Nonetheless, the thermodynamically stable orthorhombic (α-MoO_3) structure has attracted huge interest because of its many uses, including gas sensors,[38] catalysts,[39] lubricants,[40] photochromic and electrochromic devices,[41] solar cells,[42] batteries[43] and SCs.[17,18] The 1-D nanostructured morphologies, together with nanorods, nanobelts, nanotubes, nanofibers, and nanowires, have huge surface areas that are easily accessible and short diffusion routes that allow for the passage of electrons and ions to provide high capacitance and better electrochemical characteristics.[44] The present study emphasizes on the 1-D nanostructure of MoO_3 (nanobelts). Many reports have already been made on MoO_3 nanoplates,[45] nanowires,[46] and nanorods[47] as electrode materials for SCs.

Although MoO_3 has attractive characteristics, its low conductivity and tendency to undergo structural breakdown into aqueous electrolyte obstruct its performance and long-term cycling stability in electrochemical devices.[17,48,49] To address these problems, several researchers have attempted to fabricate MoO_3 nanostructures and have improved their physicochemical characteristics using a variety of approaches. The usual way to improve the capacitive properties of MoO_3 electrodes is to involve the synthesis of MoO_3-based organic and inorganic nanocomposites. Currently, metal oxide-incorporating MoO_3 nanocomposites have gained a lot of attention due to their improved cycling stability and collective pseudocapacitance contributions.[50–53] Researchers have extensively studied TMOs, such as cadmium oxide (CdO), for SC application due to their high conductivity, cost-effectiveness, eco-friendliness, and good structure.[54,55] Nonetheless, the typical electrical conductivity of CdO does not meet the requirements for high-performance SCs. Therefore, it is crucial to develop composites of CdO with various nanomaterials, as this could enhance energy storage capabilities.[56] For instance, Wang *et al.*[57] fabricated Co_3O_4/CdO nanocomposites for SCs by a solvothermal method. The synthesized material has a specific capacitance (C_s) of 351.2 F g^{-1} at 2 A g^{-1} and a capacitive retention of 84.9% at 10 A g^{-1}. Althubiti *et al.*[56] prepared CdO-doped ZnSe electrodes through a hydrothermal method. They found that the C_s of the fabricated nanocomposite material is about 1006.8 F g^{-1} at 1 A g^{-1} and 92% retention rate. Kenesi *et al.*[58] prepared a ternary nanocomposite electrode material *via* a co-precipitation method. They found a C_s of 647 F g^{-1} at 1 A g^{-1} and a stability of 82% after 500 cycles. Anwar *et al.*[59] have synthesized PANI/CdO composites using the *in situ* chemical polymerization route. The PANI-5%CdO nanocomposite exhibited a higher C_s of 906.8 F g^{-1} at 9.26 A g^{-1}. Sivaram *et al.*[60] prepared a PbO/CdO composite electrode material for SCs which exhibited a higher C_s of 300 F g^{-1} at 1 A g^{-1}, while the pure PbO exhibited 124 F g^{-1} only. The observed capacitance retention of PbO/CdO is 90% following 5000 cycles. Sivasamy *et al.*[61] fabricated a Gd_2O_3/CdO composite by the sol–gel method and observed a C_s of 521 F g^{-1} at a scan rate of 5 mV s^{-1}.

It is perceived from the discussion above that adding CdO accelerates the electrochemical behavior of a variety of materials for a few reasons. The porous nature of CdO within the nanocomposite offers an increased surface area and a greater number of active sites. This structure can enhance the capacitance performance when in contact with the electrolyte. CdO enhances the diffusion pathways within nanocomposites, which boosts their ionic conductivity and perhaps their specific capacitance.[56,59] Therefore, the current study is an attempt at the synthesis of MoO_3/CdO nanocomposites. Although few studies have explored MoO_3/CdO nanocomposites in terms of their applications in sensing devices and radiation shielding,[62,63] the controlled integration of CdO nanoparticles into MoO_3 nanobelts remains largely unexplored for SC applications. For the highest possible performance, it is essential to comprehend the optimal CdO concentration for device applications. Thus, understanding the impact of CdO concentration on the electrochemical performance of MoO_3 is required. This study aims to develop an appropriate electrode material based on a MoO_3/CdO nanocomposite by varying the concentration of CdO that will enhance the redox activity of SCs through a synergistic effect. The findings of this work could offer beneficial perspectives on designing efficient hybrid electrode materials, contributing to the improvement of next-generation energy storage devices.

Several techniques have been established to synthesize MoO_3. Here, a facile hydrothermal technique was introduced for the synthesis of the MoO_3/CdO nanocomposite as SC electrode materials because of its unique characteristics, which include low cost, moderate reaction temperature, easy control over crystal size and structure, homogenous precipitation, convenient operation, and environmental friendliness.[64] This study presents a comprehensive analysis of how varying CdO concentrations influence the physical and electrochemical characteristics of the fabricated electrode materials by usual characterization techniques.

2. Materials and methods

2.1. Materials

Analytically pure chemical reagents were used with no further refinement. Sodium molybdate dihydrate ($Na_2MoO_4 \cdot 2H_2O$, ≥

 © 2025 The Author(s). Published by the Royal Society of Chemistry

Open Access Article. Published on 22 July 2025. Downloaded on 12/8/2025 6:04:23 AM. This article is licensed under a Creative Commons Attribution-NonCommercial 3.0 Unported Licence.

99%) was obtained from Sigma-Aldrich, USA. Cadmium acetate dihydrate ($Cd(CH_3COO)_2 \cdot 2H_2O$, 98%) and hydrazine hydrate ($N_2H_4 \cdot H_2O$, 80%) were obtained from Research Lab, India. Hydrochloric acid (HCl (37%), 35.90%) was received from VWR, USA. Dimethyl sulfoxide (DMSO) ($(CH_3)_2SO$, 99%) was obtained from SRL, India. Polyvinyl alcohol (PVA) ($[CH_2CH(OH)]_n$, 99%) and sodium sulfate (Na_2SO_4, ≥99%) were received from Research Lab, India. High-purity deionized water (DIW) was used during the research.

2.2. Sample preparation

A one-step hydrothermal approach was employed to synthesize MoO_3, CdO, and MoO_3/CdO nanocomposites.

2.2.1. Synthesis of MoO_3 nanobelts. Initially, 120 ml of DIW was added to 0.08 M $Na_2MoO_4 \cdot 2H_2O$ and the mixture was continuously stirred while HCl (37%, ~3 ml) was added drop by drop to keep the pH level between 0 and 1 (pH < 1). The precursor solution was continuously stirred for 30 min before being placed into an autoclave. It was then heated to 150 °C for 24 hours, and cooled to room temperature. Following centrifugation, the precipitate was thoroughly washed multiple times with ethanol and DIW to eliminate impurities. Subsequently, the washed precipitates were dried overnight in an oven set at 60 °C.

2.2.2. Synthesis of CdO nanoparticles. Initially, $Cd(CH_3COO)_2 \cdot 2H_2O$ (0.25 M) was melted in 100 ml of DIW under continuous stirring. Hydrazine hydrate (~5 ml) was then added dropwise to maintain the pH at around 9, followed by stirring for 30 min. Afterward, the mixture was placed in an autoclave chamber and heated at 150 °C for 12 hours. Once cooled to room temperature, the precipitate was obtained through centrifugation and repeatedly washed with DIW and ethanol. The resulting product was dried overnight at 60 °C and, finally, annealed at 400 °C for 3 hours in a furnace.

2.2.3. Synthesis of MoO_3/CdO nanocomposites. For the preparation of MoO_3/CdO nanocomposites, different weight percentages of CdO (1 wt%, 3 wt%, and 5 wt%) were incorporated into MoO_3 and labeled as MoO_3/CdO (1%), MoO_3/CdO (3%), and MoO_3/CdO (5%), respectively. To prepare MoO_3/CdO, at first, CdO was prepared by a similar method mentioned in Section 2.2.2. Then, a suitable amount of CdO nanoparticles was dissolved in 20 ml DIW using bath sonication for 1 hour (solution A). Meanwhile, $Na_2MoO_4 \cdot 2H_2O$ (0.08 M) was melted in 100 ml DIW and stirred for 30 minutes, while HCl (37%, ~3 ml) was added drop by drop to keep the pH level between 0 and 1 (pH < 1) (solution B). Once homogeneous, the solutions A and B were mixed and vigorously stirred for 10 minutes. The mixture was then placed into an autoclave and heated at 150 °C for 24 hours. After being cooled to room temperature, the resulting precipitate was centrifuged and washed three times with ethanol and DIW to remove impurities. After overnight drying at 60 °C, the washed precipitates were finely ground into a powder. The synthesis was conducted without the use of surfactants or binders; however, the stable dispersion of nanomaterials was effectively achieved through pH control. The hydrothermal conditions promoted the formation of CdO nanoparticles on MoO_3, thereby ensuring excellent composite stability. A synthesis scheme of MoO_3, CdO, and MoO_3/CdO nanocomposites is presented in Fig. 1.

2.3. Materials characterization

The structural properties of the synthesized nanomaterials, including the phase structure, were examined using X-ray diffraction (XRD) analysis. An X-ray diffractometer [3040 XPert PRO, Philips] operating with Cu K_α radiation of wavelength λ = 1.5406 Å was employed to examine the diffraction peaks. The surface morphology of MoO_3, CdO, and MoO_3/CdO was investigated using field emission scanning electron microscopy (FE-SEM) (JEOL, JSM, 7600F). The FE-SEM images were analyzed using ImageJ software. The MATLAB software was used for porosity calculation from the FE-SEM images. The elemental composition and elemental mapping of the samples were analyzed using energy dispersive X-ray spectroscopy (EDS) integrated with FE-SEM.

2.3.1. Electrode preparation. Initially, a semi-liquid mixture containing the synthesized samples (70 mg) as the electrode material, DMSO as the solvent, and PVA (4 wt% of the active material) as the binder was prepared. PVA serves as an excellent binder for high-capacity electrodes due to its numerous hydroxyl groups, which may create strong hydrogen bonds with the active materials as well as the current collector.[65] Achieving a homogeneous slurry required approximately 60 min of sonication. Subsequently, this slurry was evenly deposited onto the cleaned surface of a modified graphite rod by using a micropipette. The active electrode materials had an average mass loading of 0.3 mg, while the area of the modified graphite electrode is 0.5 cm^2. The mass of the electrode material (m) was measured by comparing the electrode's weight before and after deposition. The electrodes were then allowed to dry for a few hours at 60 °C to be used as current collectors during the tests. For the electrolyte preparation, the appropriate amount of Na_2SO_4 was mixed with DIW and stirred for 10 min to ensure uniformity.

2.3.2. Electrochemical measurements. A CS310 electrochemical workstation (Corrtest, China) was used to evaluate the electrochemical performance of the synthesized materials. Various investigation methods, including cyclic voltammetry (CV), galvanostatic charge–discharge (GCD), electrochemical impedance spectroscopy (EIS), and cycling stability, are used. These measurements were conducted using a three-electrode system in a 0.5 M Na_2SO_4 solution. Na_2SO_4 serves as a neutral aqueous electrolyte, providing high conductivity and effectively preventing the corrosion of transition metal oxide electrodes, which contribute to long-term stability and safety.[66,67] The EIS measurements were executed using a sinusoidal signal within 0.1 Hz to 1 MHz frequency range. The modified graphite electrode, onto which the active material was deposited, functioned as a working electrode or current collector. A platinum wire served as the counter electrode, whereas an Ag/AgCl/saturated KCl electrode was utilized as the reference electrode. From the GCD results and the following equation, the specific capacitance (C_s) was determined.[68,69]

Open Access Article. Published on 22 July 2025. Downloaded on 12/8/2025 6:04:23 AM.
This article is licensed under a Creative Commons Attribution-NonCommercial 3.0 Unported Licence.

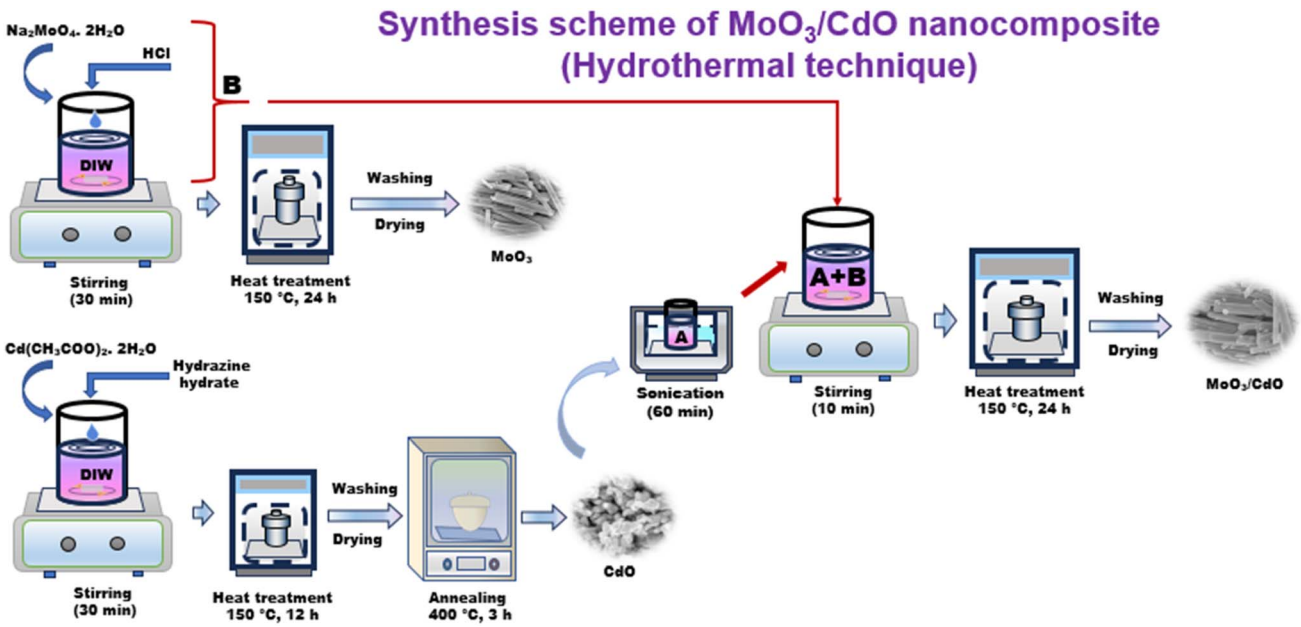

Fig. 1 Schematic illustration depicting the synthesis of MoO_3, CdO, and MoO_3/CdO (different wt%) nanocomposites by the hydrothermal technique.

$$C_s(\mathrm{F\ g^{-1}}) = \frac{I \times \Delta t}{m \times \Delta V} \quad (1)$$

In this context, I signifies the discharge current (A), Δt represents the discharge time (s), ΔV refers to the potential window (V), and m denotes the mass (g) of the active materials.

A two-electrode setup was employed to assess the practical applicability of the synthesised materials as active electrode components. Symmetric supercapacitors (SSCs) were fabricated with modified graphite electrodes for both the anode and cathode. The active materials were applied as a slurry onto the modified graphite electrodes, with the mass loading carefully adjusted to 0.6 mg per 0.5 cm^2 during electrode preparation.

3. Results and discussion

3.1. Structural properties

The crystal structures of the prepared electrode materials, including MoO_3 and MoO_3/CdO nanocomposites, were studied using XRD spectra. The XRD patterns are presented in Fig. 2(a). These spectra were also analyzed to determine the various phases and assess the purity of the samples. The XRD pattern of

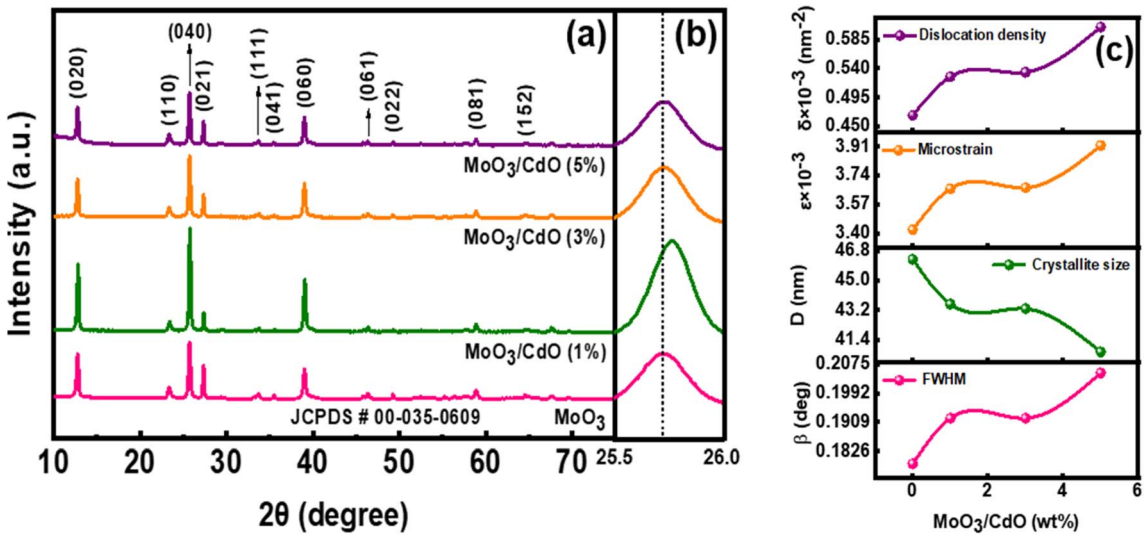

Fig. 2 (a) XRD patterns of MoO_3 and MoO_3/CdO nanocomposites, (b) zoom in view of the selected part of the XRD battern, and (c) different XRD parameters for the synthesized nanocomposites.

 © 2025 The Author(s). Published by the Royal Society of Chemistry

Open Access Article. Published on 22 July 2025. Downloaded on 12/8/2025 6:04:23 AM.
This article is licensed under a Creative Commons Attribution-NonCommercial 3.0 Unported Licence.

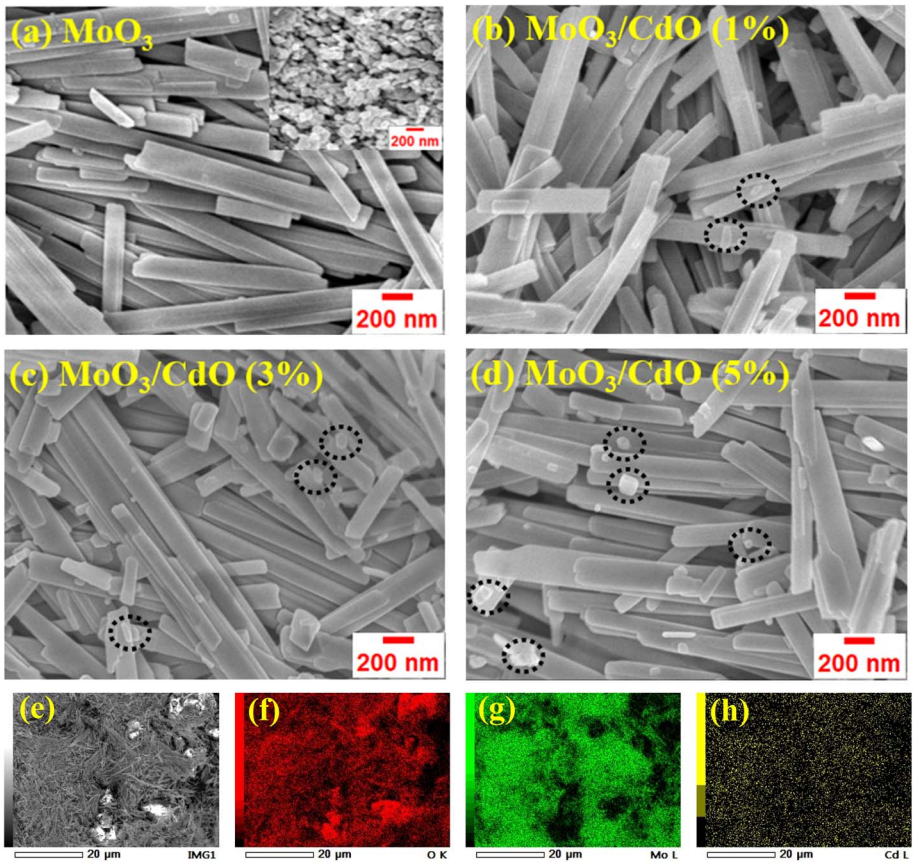

Fig. 3 FE-SEM image of the (a) MoO_3 nanobelt (CdO nanoparticle in the inset), (b) MoO_3/CdO (1%), (c) MoO_3/CdO (3%), (d) MoO_3/CdO (5%), (e) EDS elemental mapping of MoO_3/CdO (3%) from scanning electron microscope (SEM) analysis, (f) O element, (g) Mo element, and (h) Cd element.

MoO_3 shows prominent peaks at 2θ values of 12.77°, 25.70°, 27.33°, and 38.99°, which correspond to the (020), (040), (021), and (060) crystal planes, respectively. The obtained XRD pattern, not only aligned with the prominent peaks but also matched well with the minor peaks at 23.35°, 33.62°, 35.55°, 46.26°, 49.17°, 58.88° and 64.53°, which correspond to the (110), (111), (041), (061), (022), (081) and (152) planes, respectively. The comparison of the XRD pattern with the standard reference data (JCPDS#00-035-0609) verifies the successful formation of MoO_3.[70] The obtained lattice parameters were a = 3.963 Å, b = 13.856 Å, and c = 3.969 Å, confirming that the synthesized MoO_3 exhibits an orthorhombic structure with a *P*bnm space group.[70] No further impurity peaks were perceived in the XRD spectra, demonstrating that the material exhibited high purity, confirming the stability of the orthorhombic structure in the resulting samples. The diffraction peaks of CdO (ESI Fig. S1†) are noted at 2θ values of 33.05°, 38.29°, 55.27°, 65.9°, and 69.24°, which are indexed as (111), (200), (220), (311) and (222) reflections of the crystalline cubic phase of CdO. The values align closely with the standard data (JCPDS #01-075-0592).[71] The diffraction patterns of nanocomposites are similar to those of MoO_3, with no distinct diffraction peaks of CdO observed in the XRD pattern. This could be attributed to the low concentration of the incorporated CdO within the MoO_3 crystal structure.[72] This suggests that the crystalline structure remains unchanged despite the incorporation of CdO.

However, from Fig. 2(a), a shift in the primary position of the peak is observed. Fig. 2(b) shows the peak shifting of the most prominent peak (040) toward higher 2θ values upon CdO incorporation. This shift suggests a reduction in interplanar spacing (d-spacing) and a corresponding compression of the lattice cell volume.[73] The observed peak shift may arise from the variation in ionic radii of the dopant Cd^{2+} (0.78 Å)[74] and that of Mo^{6+} (0.59 Å).[75] Due to the difference in ionic radii, the incorporation of CdO may generate internal stress or trigger structural rearrangement within the MoO_3 lattice. The substitutional doping or interstitial incorporation of CdO may force adjacent Mo–O bonds to compress, driven by modifications in bond angles.[76] The resulting compression can enhance electronic conductivity. Following the incorporation of CdO, the intensity of the diffraction peak, particularly the (040) peak, increases and becomes sharper for the MoO_3/CdO (1%) and MoO_3/CdO (3%) nanocomposites. In contrast, the peak intensity decreases and broadens for the MoO_3/CdO (5%) nanocomposites. Broader and less intense diffraction peaks indicate smaller crystallite sizes and reduced crystallinity, whereas narrower and higher intense peaks indicate larger crystallite sizes and higher crystallinity.[77] Strain may develop in the MoO_3 lattice upon the

Open Access Article. Published on 22 July 2025. Downloaded on 12/8/2025 6:04:23 AM. This article is licensed under a Creative Commons Attribution-NonCommercial 3.0 Unported Licence.

incorporation of Cd^{2+}, likely due to the variation in ionic radii of Cd^{2+} and Mo^{6+} ions.[78,79] Various structural parameters derived from the XRD spectra were analyzed and summarized in ESI Table S1,† with a graphical representation provided in Fig. 2(c). The Debye–Scherrer formula was employed to calculate the average crystallite size (D).[80]

$$D = \frac{K\lambda}{\beta\cos\theta} \tag{2}$$

The calculation of microstrain was performed using the following equation.

$$\varepsilon = \frac{\beta}{4\tan\theta} \tag{3}$$

In this context, λ signifies the wavelength of the X-ray employed, β indicates the broadening of the diffraction line or the full width at half maximum (FWHM) measured in radians, and θ represents the diffraction angle (in degrees) at the peak of most significant intensity. $K = 0.90$ is the shape factor (an arbitrary), also known as Scherrer's constant. The (040) plane was selected for measuring the crystallite size. With an increase in CdO concentration, the crystallite size decreases, while the microstrain values increase. The increase in microstrain suggests an enhancement in lattice imperfections, such as dislocations, structural defects, and vacancies, which facilitates faster ion diffusion on the electrode surface.[81] The obtained crystallite size (D) is used to determine the dislocation density.[80]

$$\delta = \frac{1}{D^2} \tag{4}$$

The dislocation density of the samples is influenced by the increase in doping concentration and increases with the incorporation of CdO. This reflects the presence of imperfections in the composite materials and facilitates the rapid transport of electrons from the active sites to the electrodes.[82] Changes in XRD peak positions suggest lattice distortion resulting from the interaction between the two phases. Fluctuations in crystallite size indicate alterations in nucleation and growth dynamics influenced by the secondary phase. Variations in microstrain and dislocation density indicate structural alterations aligned with the development of composite or heterostructure formations.

3.2. Surface morphology

The micrograph of MoO_3 and MoO_3/CdO nanocomposites is presented in Fig. 3. The MoO_3 micrograph (Fig. 3(a)) reveals one-dimensional (1-D) nanobelt structures with an average length of 0.8–3.2 μm and an average width of around 100–228 nm. The 1-D nanostructured morphologies are easily accessible and have short diffusion routes to allow the passage of electrons and ions.[44] The morphology of CdO consists of nanoparticles, as shown in the inset of Fig. 3(a). The size of these nanoparticles varies between 34 and 76 nm. Fig. 3(b–d) shows FE-SEM micrographs of the synthesized MoO_3/CdO nanocomposites. The CdO nanoparticles (dashed circle) are found to be distributed randomly on the surface of MoO_3 nanobelts. These micrographs are quite similar to those of the MoO_3 nanobelts because of the low concentration of CdO. However, the length of the nanobelts reduces as the doping concentration increases, which lowers their aspect ratio. Structures with low aspect ratios typically provide shorter diffusion pathways, facilitating faster ion transport, and are less susceptible to structural failure.[79] ESI Fig. S2(a–d) and S3(a–d)† display the pore structure and pore volume distribution of the synthesized nanomaterials. MATLAB software and volume-based methods were employed for porosity analysis.[83]

The graphical representation in ESI Fig. S4† shows the percentage of porosity of MoO_3 as a function of increasing concentration of the CdO nanoparticles. The addition of CdO nanoparticles leads to reduced porosity in the CdO-incorporating MoO_3 nanocomposite (Fig. S4†). This reduced porosity may arise from the incorporation of CdO nanoparticles into the interstitial spaces of the MoO_3 crystal structure, leading to a higher packing density. Efficient ion transport channels remain accessible at elevated packing densities in electrode materials, resulting in enhanced electrochemical performance and improved cycling stability.[84,85]

The EDS data provided insights into the chemical composition of the nanocomposites, as illustrated in Fig. S5.† The EDS data reveal the presence of O, Mo, and Cd elements, which are anticipated in MoO_3/CdO composites. The observed increase in Cd content within the composites upon the addition of CdO confirms the effective integration of CdO into MoO_3, as detailed in Table S2.† Alongside the elemental composition, the characterization through elemental mapping reveals a consistent spatial distribution of O, Mo, and Cd throughout the nanocomposites. The elemental mapping for a representative sample, specifically the MoO_3/CdO composite, is illustrated in Fig. 3(e–h). The EDS mapping is evidence for composite or heterostructure formation.

3.3. Electrochemical properties

To evaluate the electrochemical performance of the synthesized nanomaterials as active electrodes for SCs, the CV, GCD, and EIS analyses were performed in 0.5 M Na_2SO_4 electrolyte solution using a three-electrode system. There are two different ways that materials can hold charges. The first way involves faradaic charge transfer, known as "pseudocapacitance," where metal cations from the electrolyte (in this case, Na^+) diffuse into the MoO_3 layers and intercalate with them.

$$MoO_3 + Na^+ + e^- \rightleftharpoons MoO_3Na \tag{5a}$$

The second technique for storing charge arises from a non-faradaic process, where charges gather at the electrode/electrolyte interface, forming an electric double layer.[86,87]

$$(MoO_3)_{surface} + Na^+ + e- \rightleftharpoons (MoO_3{}^-Na^+)_{surface} \tag{5b}$$

3.3.1. Cyclic voltammetry (CV). CV curves of MoO_3 and MoO_3/CdO nanocomposites were recorded at various scan rates

 © 2025 The Author(s). Published by the Royal Society of Chemistry

Open Access Article. Published on 22 July 2025. Downloaded on 12/8/2025 6:04:23 AM.
This article is licensed under a Creative Commons Attribution-NonCommercial 3.0 Unported Licence.

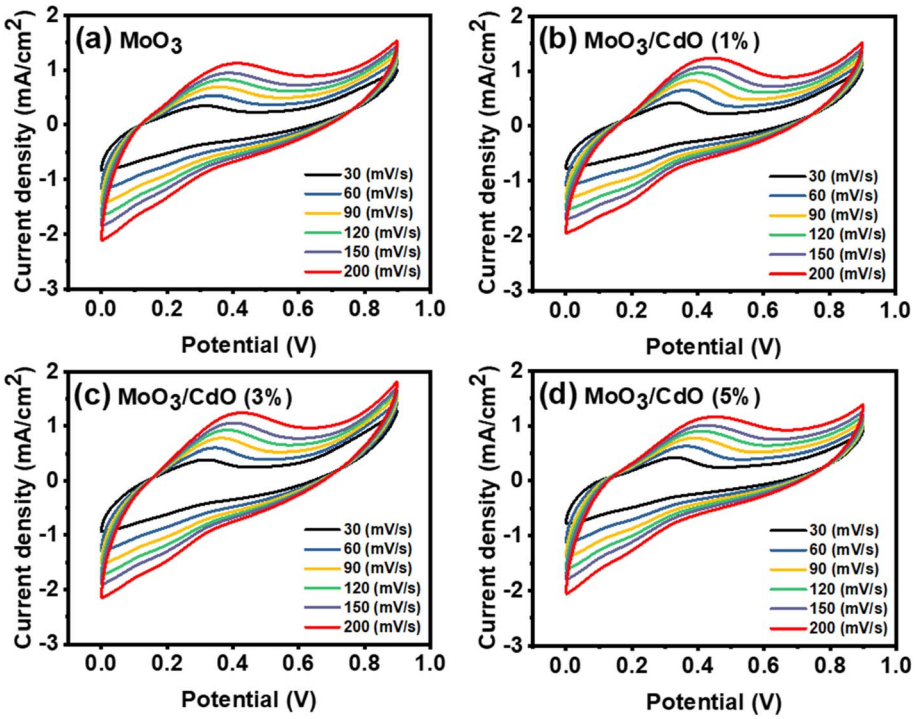

Fig. 4 CV profiles for (a) MoO_3, (b) MoO_3/CdO (1%), (c) MoO_3/CdO (3%), and (d) MoO_3/CdO (5%) at different scan rates.

(30, 60, 90, 120, 150, and 200 mV s^{-1}) using a conventional three-electrode setup within a potential window of 0 to 0.9 V and are presented in Fig. 4(a–d). In electrolytes, Na^+ ions play a crucial role in facilitating the electrochemical reaction.[88,89] A perfectly rectangular shape and symmetric current response in the CV curves signify a purely electrical double-layer capacitance storage mechanism. However, the deviance from the rectangular shape, as shown in Fig. 4(a–d), indicates the presence of a faradaic pseudocapacitive charge storage mechanism.[90] In this instance, the electrode materials in a Na_2SO_4 electrolyte exhibited oxidation and reduction processes attributed to the intercalation and de-intercalation of Na^+ ions in active materials. The appearance of a smaller oxidation peak, resulting from faradaic redox reactions, confirmed that the synthesized material exhibited pseudocapacitive behavior.[91]

The intensity of the CV curve is highly reliant on the scan rate. It has been noted that the region bounded by the CV curve and the peak current intensity both increase with a higher scan rate from 30 to 200 mV s^{-1}. The anodic peaks increased their current values (peak) and were shifted to higher potentials. This is because when the scan rate increases, the internal diffusion resistance of the pseudoactive material increases as well, or due to the kinetic irreversibility and electric polarization of ions at the electrode surface by the electrolyte during redox reactions at high scan rates.[92,93]

Moreover, with increasing scan rates, the CV curves maintain a consistent shape, demonstrating significant pseudocapacitive characteristics and impressive rate capability of the MoO_3/CdO nanocomposite.[86] The MoO_3/CdO (3%) nanocomposite exhibits a larger integral area at any given scan rate, attributed to the synergistic interactions among the metal ions in the electrode materials, surpassing the performance of other composites.[94] This suggests that the particular concentration of CdO has enhanced the capacity of the electrode for charge storage by strengthening the bond between the electrolytes and the electrochemically active components. This results in accelerated diffusion pathways for ion and electron transport, which enhances specific capacitance and makes it appropriate for energy storage applications.

3.3.1.1 Capacitive and diffusive properties. The electrochemical charge storage mechanism of the fabricated electrodes was examined through CV curves obtained at various scan rates, facilitating the estimation of current contributions from surface and diffusion-controlled processes. The general power law relationship typically observed between peak current density $i(V)$ at a specific potential V and scan rates v of CV data can be expressed as follows,[95] and termed as Dunn's model.

$$i(V) = av^b \tag{6}$$

$$\text{Or, } \log(i(V)) = \log(a) + b \times \log(v) \tag{7}$$

Both 'a' and 'b' are adjustable parameters. The parameter 'b' can be determined by analyzing the slope of the graph of $\log(i(V))$ *versus* $\log(v)$, as represented in Fig. 5(a). When the value of 'b' approaches 0.5, the electrochemical redox reaction of the electrode is predominantly governed by a diffusion-controlled mechanism, driven by faradaic ion insertion and extraction. This behavior is characteristic of typical battery-like systems. However, the capacitive behavior is dominated when the 'b' value is close to 1.[96,97] As shown in Fig. 5(a), the b-values vary

Open Access Article. Published on 22 July 2025. Downloaded on 12/8/2025 6:04:23 AM.
This article is licensed under a Creative Commons Attribution-NonCommercial 3.0 Unported Licence.

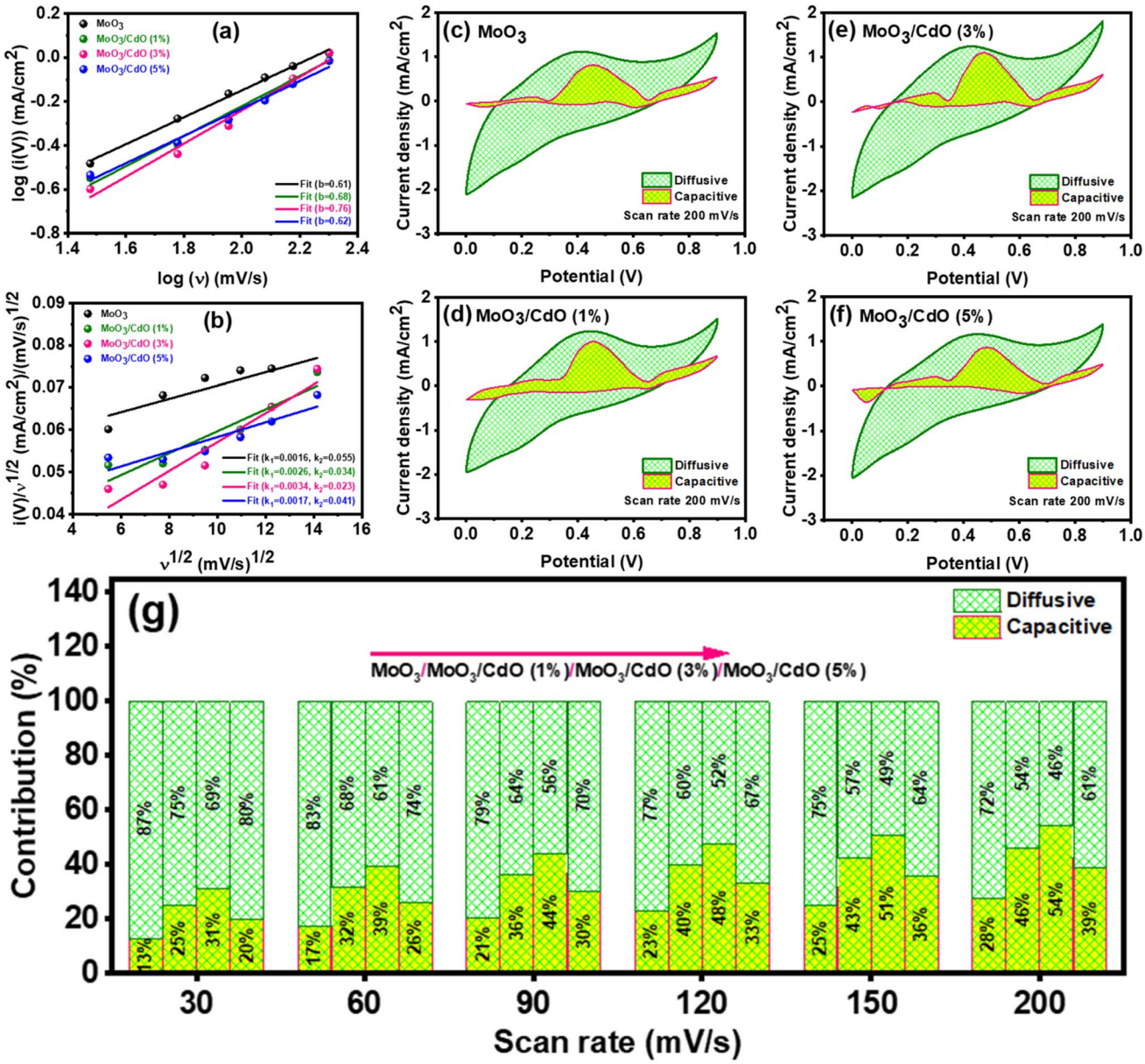

Fig. 5 (a) The determination of b-value from CV analysis through the linear plot of log($i(V)$) and log(v), (b) the plot of $i(V)/v^{1/2}$ *versus* $v^{1/2}$, (c–f) representative CV curves showing the capacitive and diffusive contributions at 200 mV s^{-1}, and (g) bar plots showing the proportions of capacitive and diffusive contributions at different scan rates for MoO_3 and fabricated nanocomposites, respectively.

from 0.61 to 0.76, particularly 0.61 for MoO_3, 0.68 for MoO_3/CdO (1%), 0.76 for MoO_3/CdO (3%), and 0.62 for MoO_3/CdO (5%) electrode materials, indicating the involvement of both capacitive and diffusion-controlled mechanisms. The b-value increases since surface processes, such as faradaic reactions or ion adsorption, are quicker and not dependent on ion diffusion.[98] Furthermore, their respective contribution rates were measured using the following equations to assess the specific contributions of the diffusion and capacitive controlled processes to the electrochemical reaction.[99]

$$i(V) = i_{\text{capacitive}} + i_{\text{diffusive}} = k_1 v + k_2 v^{1/2} \quad (8)$$

$$\text{Or } i(V)/v^{1/2} = k_1 v^{1/2} + k_2, \quad (9)$$

In this formulation, $i_{\text{capacitive}} = k_1 v$ represents the capacitive contribution, associated with a fast-kinetics process characteristic of electric double-layer capacitance. In contrast, $i_{\text{diffusive}} = k_2 v^{1/2}$ describes the diffusive current contribution, corresponding to a slower-kinetics process related to pseudo-capacitance.[100] Both k_1 and k_2 are computable parameters, determined from the slope and intercept of the linear plot of $i(V)/v^{1/2}$ *versus* $v^{1/2}$, as shown in Fig. 5(b). Once the values of k_1 and k_2 are known, it is easy to distinguish the current contribution at each potential through diffusion-controlled and capacitive processes.

 © 2025 The Author(s). Published by the Royal Society of Chemistry

Open Access Article. Published on 22 July 2025. Downloaded on 12/8/2025 6:04:23 AM.
This article is licensed under a Creative Commons Attribution-NonCommercial 3.0 Unported Licence.

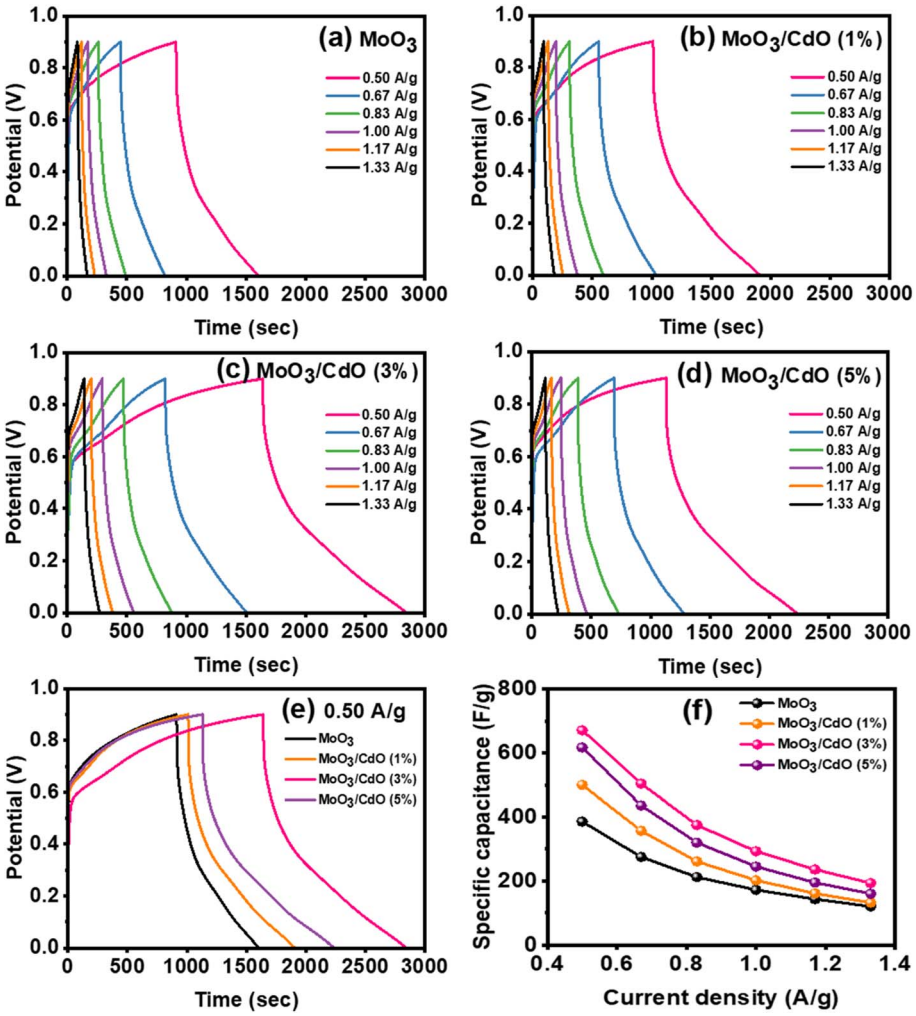

Fig. 6 GCD curves for (a) MoO_3, (b) MoO_3/CdO (1%), (c) MoO_3/CdO (3%), and (d) MoO_3/CdO (5%) nanocomposites at various current densities, (e) GCD curve of different samples at a current density of 0.5 A g^{-1}, and (f) variation of specific capacitance with current densities.

Fig. 5(c–f) present the CV plots depicting the overall contribution, including diffusive and capacitive components, for MoO_3 and other nanocomposite electrodes at 200 mV s^{-1}. Fig. 5(g) displays the charge storage percentage contributions of the capacitive (yellow color) and diffusive processes (green color). The diffusive proportions of the MoO_3 electrode are 87%, 83%, 79%, 77%, 75% and 72% at the scan rate of 30, 60, 90, 120, 150, and 200 mV s^{-1}, respectively, and those for the MoO_3/CdO (3%) electrode are 69%, 61%, 56%, 52%, 49%, and 46% at 30, 60, 90, 120, 150, and 200 mV s^{-1}, respectively. The result shows that the diffusive contribution significantly exceeds the capacitive contribution, indicating that charge storage is predominantly governed by the diffusive process, characteristic of pseudo-capacitive behavior. The capacitive contribution increases with higher scan rates, reaching 54% at 200 mV s^{-1} for the MoO_3/CdO (3%) electrode. With an increase in the scan rate and concentration of CdO, there is a decrease in the diffusion-controlled contribution, attributed to the limited time available for ion diffusion during the oxidation/reduction process into the host lattices. The rapid adsorption and desorption of electrolyte ions occur close to the electrode and electrolyte interface. This reduction in diffusion suggests that the capacitance contribution decreases due to the pseudo-capacitive mechanism at higher scan rates and higher concentrations of CdO. At low scan rates, the diffusion process prevails over the capacitive mechanism, indicating that the elevated specific capacitance of the MoO_3 electrode is mostly attributable to its pseudo-capacitive characteristics.[86,98,99]

3.3.2. Galvanostatic charge–discharge (GCD). The electrochemical performance of the synthesized materials was further assessed through GCD analysis across a potential range of 0 to 0.9 V at different current densities of 0.50, 0.67, 0.83, 1.00, 1.17, and 1.33 A g^{-1}. The GCD curves for the prepared nanomaterials are presented in Fig. 6(a–d). It is evident that none of the electrodes exhibit linear behavior, and the GCD curves deviate from the perfectly symmetric triangular shape. This deviation is attributed to the reversible conversion reaction, indicating pseudo-capacitive charge storage behavior of the fabricated electrode materials, consistent with the observations from the CV analysis.[90] Furthermore, the discharge time reduces as the

Open Access Article. Published on 22 July 2025. Downloaded on 12/8/2025 6:04:23 AM.
This article is licensed under a Creative Commons Attribution-NonCommercial 3.0 Unported Licence.

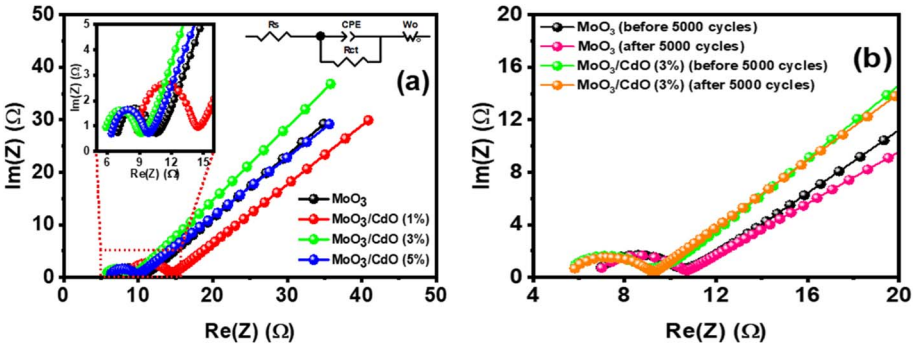

Fig. 7 (a) Nyquist plots for MoO_3 and MoO_3/CdO nanocomposites in 0.5 M Na_2SO_4 electrolytes. The inset of the figure shows an equivalent circuit used for simulation and an expanded view of the high-frequency region. (b) Comparison of Nyquist plots for MoO_3 and MoO_3/CdO (3%) electrodes before and after 5000 charge–discharge cycles.

current density increases. The electrodes require more time to discharge at reduced discharge currents, suggesting an increased charge storage capacity. Fig. 6(e) presents the comparative GCD profiles of the MoO_3 and MoO_3/CdO electrodes at an identical current density of 0.5 A g^{-1}. Among them, the MoO_3/CdO (3%) electrode displays a longer discharge time than the others.

Although CV curves provide qualitative insight into redox activity, the specific capacitance (C_s) values reported were obtained from GCD analysis using eqn (1), which offers more precise quantification of charge storage. GCD applies a constant current during both charging and discharging, leading to a voltage–time profile that is nearly linear. The linearity facilitates precise capacitance calculations through the discharge slope, reducing errors that may arise from varying current levels. In contrast, CV implies a fluctuating current as the voltage fluctuates linearly, resulting in a non-constant current that complicates precise interpretation for capacitance calculation.[101] Fig. 6(f) and ESI Table S3† present C_s at various current densities. The findings suggest that C_s diminishes as current density increases, probably because of increased polarizability and insufficient time for electrolyte ions to penetrate the inner pores of the electrode material.[56,102] The reduction in C_s values at higher current densities is mainly associated with volume expansion caused by successive multi-electron electrochemical reactions.[98]

The MoO_3/CdO (3%) nanocomposite achieved the highest C_s of 671 F g^{-1} at a current density of 0.50 A g^{-1} compared to pristine-MoO_3 (C_s of 386 F g^{-1} at 0.50 A g^{-1}). Even at higher current densities, the 3%CdO-incorporating MoO_3 electrode maintained a higher C_s than the other electrodes. This enhanced capacitance can be due to the synergistic interaction between the distinct morphological and electrically conductive characteristics of MoO_3 and CdO. In the MoO_3/CdO (3%) nanocomposite, CdO nanoparticles are better integrated with the MoO_3 nanobelts, constructing shorter diffusion pathways and better electrically conductive channels. This facilitates the electrolyte ions and electrons to migrate to the active regions of the electrodes more quickly and efficiently. Electrolytes can efficiently diffuse through nearly all available channels and pores of the active material at low current densities, enabling a complete redox reaction.

However, at high current densities, ion penetration into the innermost regions of the active material becomes limited, restricting diffusion to more accessible areas and thereby reducing the specific capacitance.[103] Although the incorporation of CdO improves the specific capacitance of MoO_3, after a certain amount, it might cause particle aggregation and increased resistance against electron mobility between the interfaces, which will ultimately result in a slight decrease in capacitance for the MoO_3/CdO (5%) electrode.[104,105]

3.3.3. Electrochemical impedance spectroscopy (EIS). The charge transfer dynamics of the synthesized nanomaterials were examined through EIS analysis. This technique is highly effective for gaining information about the electrochemical impedance characteristics of the electrodes. In this study, the various fabricated electrodes were analyzed in a 0.5 M Na_2SO_4 solution. The frequency range for the analysis was set from 0.1 Hz to 1 MHz, with an alternating voltage amplitude of 10 mV at the open-circuit potential (OCP). The EIS data are displayed as Nyquist plots in Fig. 7(a), and the inset provides a magnified view of the high-frequency region. This plot reveals a single semicircle in the higher frequency range for each sample; this reflects the charge transfer procedure. The intersection of the curve with the real impedance (*x*-axis) in the high-frequency region indicates the internal resistance (R_s) of the electrochemical systems. The diameter of the semicircle represents the interfacial charge transfer resistance (R_{ct}) between the electrolyte and electrode.[88,106]

In the low-frequency range of the Nyquist plots, the inclined straight line is associated with ion diffusion within the

Table 1 Values of R_s, CPE, R_{ct}, and W_o in the three-electrode system determined through fitting with an equivalent circuit model

Sample	R_s (Ω)	CPE (μF)	R_{ct} (Ω)	W_o (Ω)
MoO_3	7.16	0.031	2.91	2.47
MoO_3/CdO (1%)	8.86	0.034	4.99	4.30
MoO_3/CdO (3%)	6.20	0.205	2.35	4.56
MoO_3/CdO (5%)	7.40	0.028	2.37	21.21

 © 2025 The Author(s). Published by the Royal Society of Chemistry

Open Access Article. Published on 22 July 2025. Downloaded on 12/8/2025 6:04:23 AM.
This article is licensed under a Creative Commons Attribution-NonCommercial 3.0 Unported Licence.

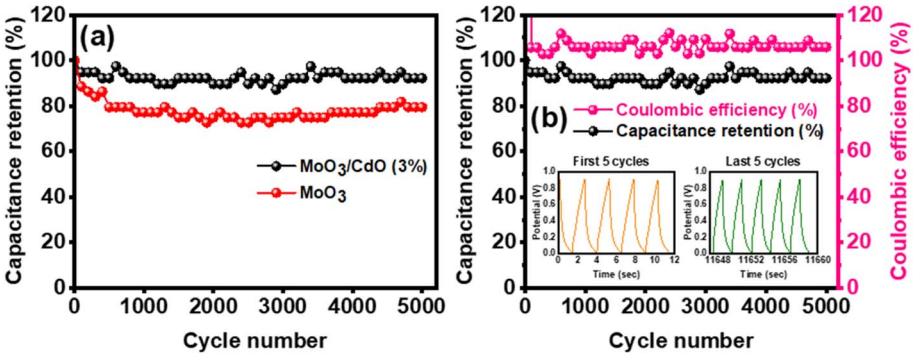

Fig. 8 (a) Capacitance retention of MoO_3 and MoO_3/CdO (3%) electrodes over 5000 cycles at a current density of 8 A g^{-1}. (b) Coulombic efficiency of the MoO_3/CdO (3%) electrode as a function of the cycle number.

electrolyte, known as Warburg impedance (W_o), which corresponds to mass transfer resistance. If the Warburg angle exceeds 45° in this region, it specifies that the ion diffusion process shows a leading role in controlling the behavior of the electrode.[107,108] An equivalent electrical circuit employed to model the EIS data is presented in the inset of Fig. 7. This circuit includes the components R_s, R_{ct}, W_o, and a constant phase element (CPE). The CPE can explain the frequency-dependent behavior of the measured capacitance.[109] Table 1 displays the charge transfer kinetic parameters of the electrodes using an equivalent electrical circuit for fitting the EIS data. The R_s value of the MoO_3/CdO (3%) electrode is notably lower than those of the other electrodes, confirming its reduced internal resistance. The radius of the Nyquist plot is generally proportional to the R_{ct}. The initially higher R_{ct} noted for MoO_3/CdO (1%) can be attributed to the lack of a percolative CdO network and suboptimal interfacial contact at this low concentration. As the CdO content increases, a continuous percolation network is established, significantly reducing R_{ct}.

From the plot, the MoO_3/CdO (3%) electrode exhibits a smaller semicircle radius, corresponding to a lower R_{ct} value of 2.35 Ω. This recommends a quicker faradaic response with significantly reduced resistance, exhibits higher ionic conductivity, and contributes to enhanced capacitive performance. The CPE value is progressively better from 0.031 to 0.205 μF with the doping of CdO, reaching its highest for the MoO_3/CdO (3%) electrode. This enhanced CPE value indicates an improved interface of the electrode/electrolyte, which may improve the superior electrochemical performance of the MoO_3/CdO nanocomposites.[110–112] As illustrated in Fig. 7, the electrode exhibits a steeper slope of Warburg impedance in the low-frequency region with increased CdO concentration, demonstrating enhanced ion diffusion within the electrode material. This indicates more efficient ion transport across the electrolyte–electrode interface, resulting in enhanced charge transfer kinetics, lower diffusion resistance, and improved overall electrochemical performance. A steeper slope often signifies greater capacitive behavior and accelerated redox reactions, thereby boosting the energy storage capability of the device.[23] All results from the EIS analysis indicate the improved ion transfer capability and conductivity of the MoO_3/CdO (3%) electrode, which is further confirmed by the CV and GCD analyses. The Nyquist plot shown in Fig. 7(b) reveals a slight increase in both R_{ct} (2.999 Ω for MoO_3, 2.41 Ω for MoO_3/CdO (3%)) and R_s (7.281 Ω for MoO_3, 6.61 Ω for MoO_3/CdO (3%)), indicating that the electrode maintains good conductivity even after 5000 charge–discharge cycles. However, the increase in R_{ct} for MoO_3/CdO (3%) was less significant compared to pure MoO_3, confirming the superior structural and electrochemical stability of the composite material.

3.3.4. Cycling stability. Cycling stability is essential for assessing the efficiency of a supercapacitor electrode. Fig. 8(a) presents the long-term cycling performance of the electrodes exhibiting the highest and lowest values of specific capacitance. Additionally, the inset displays the results of the repetitive GCD test conducted over 5000 cycles at 8 A g^{-1}, within the potential window of 0.0 to 0.9 V. The figure indicates that the MoO_3/CdO (3%) electrode material demonstrates outstanding stability over 5000 cycles, maintaining reversible capacitive behavior with approximately 92% retention, even under high charge/discharge rates. A slight decline in specific capacitance is observed through the early cycles, after which it stabilizes and remains consistent throughout the 5000 cycles. The excellent cycling stability of the MoO_3/CdO (3%) electrode can be attributed to the unique nanocomposite structure and enhanced ion diffusion at the interface.

For comparison, the cycling stability of MoO_3 electrodes was also evaluated, showing a retention of 80% after 5000 charge–discharge cycles. These findings suggest that the integration of CdO nanoparticles improves the stability of the nanocomposite. The observed decline in cycling stability could be attributed to the degradation of the MoO_3 chemical structure, the dissolution of constituent ions into the electrolyte during electrochemical processes, or capacity imbalances between the electrodes.[13,113] Metal oxide electrodes often exhibit limited cycling stability due to structural degradation occurring during redox processes.[114]

For practical applications, electrode materials are expected to demonstrate significantly high coulombic efficiency. Fig. 8(b) illustrates the change in coulombic efficiency of the MoO_3/CdO (3%) electrode over multiple cycles. The coulombic (or faradaic) efficiency was determined as the ratio of discharge time to charge time, reflecting the practical suitability of the electrode

Open Access Article. Published on 22 July 2025. Downloaded on 12/8/2025 6:04:23 AM.
This article is licensed under a Creative Commons Attribution-NonCommercial 3.0 Unported Licence.

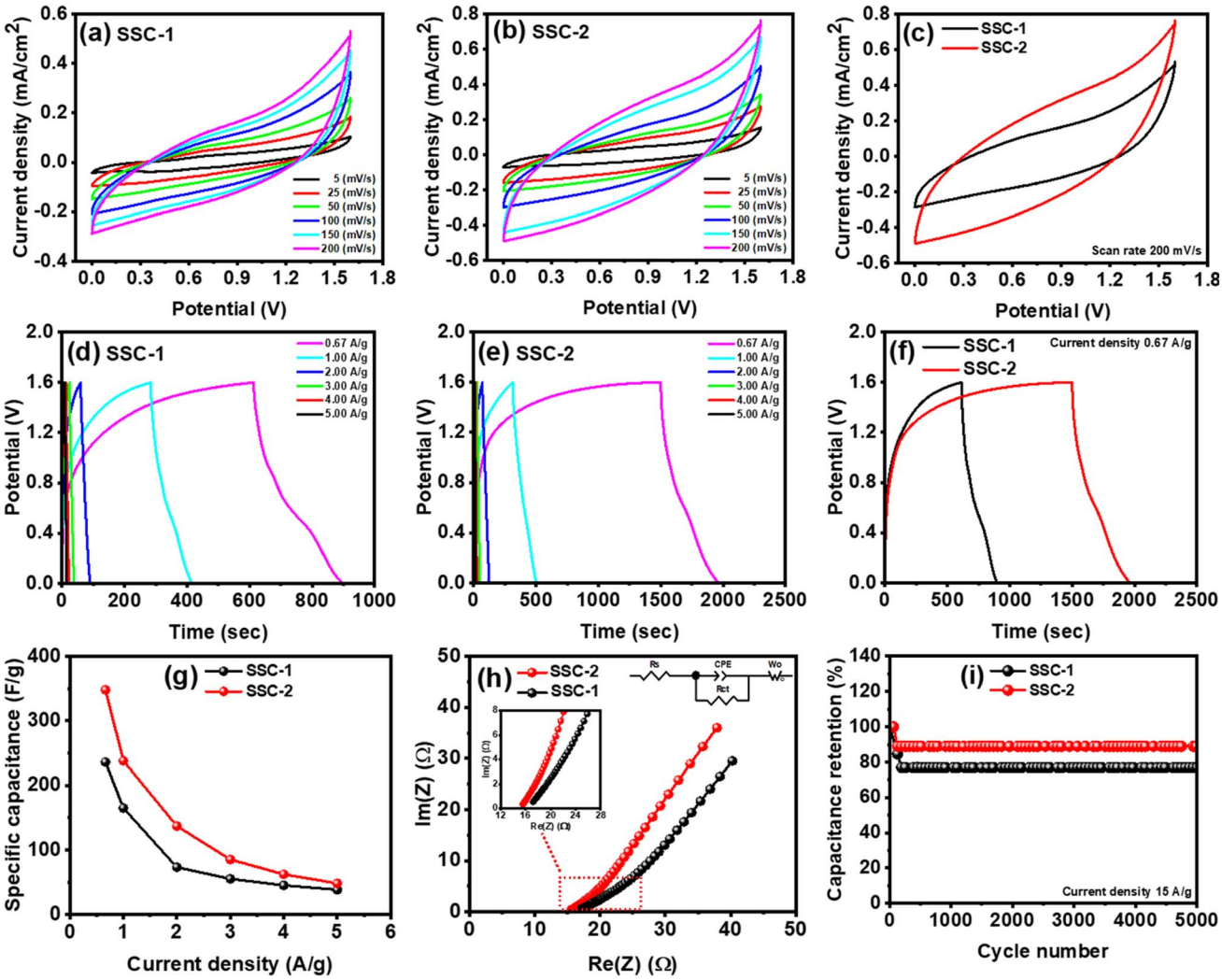

Fig. 9 Electrochemical properties of the SSC. CV profiles for (a) SSC-1 and (b) SSC-2 at different scan rates. (c) Variation of the CV curve at a scan rate of 200 mV s^{-1}. GCD profile of (d) SSC-1 and (e) SSC-2 at different current densities. (f) Variation of the GCD curve at a current density of 0.67 A g^{-1}. (g) Variation of specific capacitance with current densities. (h) Nyquist plots. The upper right inset of the figure presents an equivalent circuit used for simulation, and the lower right inset depicts an enlarged view of the high-frequency area. (i) Cycling performance over 5000 cycles at a current density of 15 A g^{-1}.

material for SCs. The high coulombic efficiency confirms the enhanced redox reversibility of the electrode material.[115] As the number of cycles increased, the coulombic efficiency exceeded 100%, reaching 106%. This phenomenon can be attributed to parasitic reactions, such as the degradation of the electrode and electrolyte, which introduce additional charges during the discharge process.[116] The high coulombic efficiency and outstanding cycling stability demonstrate the effectiveness of the MoO_3/CdO (3%) nanocomposite for use in high-performance SCs.

3.4. Symmetric supercapacitor (SSC) performance characteristics and evaluation

The SSCs, MoO_3//MoO_3 and MoO_3/CdO(3%)//MoO_3/CdO(3%), were constructed and further referred to as SSC-1 and SSC-2, respectively. For the symmetric cell configuration, the specific capacitance, C_{cell} (F g^{-1}), energy density, E (W h kg^{-1}), and power density, P (W kg^{-1}), were calculated using the following equations.[117,118]

$$C_{cell}(\mathrm{F\ g^{-1}}) = 4\left(\frac{I \times \Delta t}{M \times \Delta V}\right) = 2\left(\frac{I \times \Delta t}{m \times \Delta V}\right) \tag{10}$$

$$E(\mathrm{W\ h\ kg^{-1}}) = \frac{C_{cell} \times (\Delta V)^2}{2 \times 3.6} \tag{11}$$

$$P(\mathrm{W\ kg^{-1}}) = \frac{E}{\Delta t} \times 3600 \tag{12}$$

In this context, I (A) denotes the charge and discharge current established for the GCD test, Δt (s) signifies the duration of discharge, m (g) refers to the mass of each active material, M (g) indicates the total mass load on both electrodes, and ΔV(V)

 © 2025 The Author(s). Published by the Royal Society of Chemistry

Open Access Article. Published on 22 July 2025. Downloaded on 12/8/2025 6:04:23 AM.
This article is licensed under a Creative Commons Attribution-NonCommercial 3.0 Unported Licence.

represents the voltage window applied in the electrochemical test.

The electrochemical properties of SSCs are displayed in Fig. 9 and 10. CV curves were obtained at different scan rates ranging from 5 to 200 mV s^{-1} within the optimal potential window of 0 to 1.6 V in a 0.5 M Na_2SO_4 aqueous electrolyte, as illustrated in Fig. 9(a–b). The observation indicates that the area enclosed by the CV curve increases as the scan rate increases from 5 to 200 mV s^{-1}. As the scan rate increases, the CV profile maintains a consistent shape without any noticeable distortion, because mass transfer or ion transport of charges between the electrode and electrolyte occurs with a lack of restriction. This suggests that the symmetric configuration is kinetically reversible.[119] The comparison of CV curves of SSC-1 and SSC-2 is displayed in Fig. 9(c) at a fixed scan rate of 200 mV s^{-1}. The integrated CV area of the SSC-2 is larger than that of SSC-1, indicating a greater charge storage capacity on the surface of the SSC-2.

The GCD plots for SSC-1 and SSC-2 are conducted at varying current densities from 0.67 to 5 A g^{-1}, within a potential range of 0 to 1.6 V. Fig. 9(d–e) illustrates the nonlinear charge–discharge profiles, confirming the predominant pseudocapacitive characteristics of the SSCs. The GCD curves obtained at different current densities exhibited symmetry and consistency, demonstrating the exceptional reliability and stability of the SSC under high current densities.

Fig. 9(f) illustrates the comparative GCD profiles of SSC-1 and SSC-2 at the same applied current density of 0.67 A g^{-1}. Remarkably, compared to the SSC-1, the GCD curve of the SSC-2 shows a longer discharge time. Fig. 9(g) presents C_s at various current densities calculated from the GCD curves using eqn (10). The fabricated SSC-2 exhibits a high C_s of 348 F g^{-1} at 0.67 A g^{-1} and retains 48 F g^{-1} at 5 A g^{-1}, outperforming SSC-1 at the corresponding current densities. Even at high current densities, the SSC-2 retained larger C_s than the SSC-1. The findings suggest that C_s decreases with higher current density. At higher current densities, the fast ion insertion and extraction process restricts access to the whole surface area of the electrode, leading to less charge accumulation on the electrode surface. At a lower current density, the ions in the electrolyte fully interact with the active material, leading to a significant increase in the C_s.[120]

The charge transfer kinetics of the designed SSCs was analyzed using EIS. This method is particularly efficient for acquiring information on the electrochemical impedance properties of the electrodes. The analysis frequency range has been chosen from 0.1 Hz to 1 MHz, using an alternating voltage amplitude of 10 mV at the OCP. The EIS data are shown as Nyquist plots in Fig. 9(h), with the inset offering an enlarged viewpoint of the high-frequency area. EIS plots reflect the parameters, including charge transfer resistance (R_{ct}), equivalent series resistance (R_s), Warburg impedance, and constant phase element (CPE). Table 2 displays the charge transfer kinetics parameters of the fabricated SSCs using an equivalent electrical circuit for fitting the EIS data.

The R_s value of SSC-2 is 14.99 Ω lower than that of the SSC-1 (16.24 Ω), confirming its reduced internal resistance. SSC-2 also exhibits a lower R_{ct} value of 230.9 Ω than SSC-1 (309.7 Ω). This recommends a quicker faradaic response with significantly reduced resistance, exhibits higher ionic conductivity, and contributes to enhanced electrochemical performance. The reported resistance values for R_{ct} and R_s in a symmetrical two-electrode design are typically greater than those in a three-electrode arrangement. This is caused by the fact that current flows through both electrodes in a two-electrode system simultaneously, which lowers the current density per electrode and increases the overall measured resistance. SSC-2 exhibits a higher CPE value of 0.0050 F than SSC-1 (0.0044 F). This enhanced CPE value indicates an improved interface of the electrode/electrolyte, which may improve the superior electrochemical performance of SSC-2. Improved ion diffusion, as suggested by a steeper slope of SSC-2 (Fig. 9(h)), implies lower Warburg impedance 12.52 Ω in the low-frequency region of the Nyquist plot, indicating enhanced ionic transport.

Table 2 Charge transfer kinetics parameters of SSCs determined through fitting with an equivalent circuit model

Sample	R_s (Ω)	R_{ct} (Ω)	CPE (μF)	W_o (Ω)
SSC-1	16.24	309.7	0.0044	25.18
SSC-2	14.99	230.9	0.0050	12.52

The long-term cycle performance of the fabricated SSCs was investigated by conducting the GCD test 5000 times at a current density of 15 A g^{-1} throughout a potential range of 0 to 1.6 V, and the results are shown in Fig. 9(i). It can be observed that the SSC-1 exhibited only 76.92% capacitance retention after 5000 cycles. Such a significant reduction in capacitance indicates a degradation of the chemical structure of MoO_3 and/or the dissolution of component ions during the long charge–discharge process.[13,113] However, the SSC-2 retains 88.9% of its specific capacitance after 5000 cycles, indicating its excellent long-term cycling stability.

The operational efficiency of energy storage systems is mostly dependent upon their energy density (E) and power density (P). The energy and power density of the SSC are

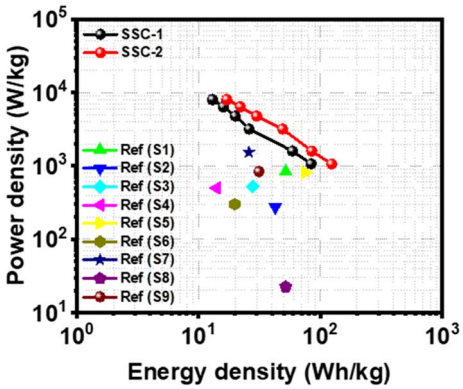

Fig. 10 Ragone plots of the fabricated SSC-1 and SSC-2 compared with reported symmetric and asymmetric SCs in the literature (for references, see the ESI†).

Open Access Article. Published on 22 July 2025. Downloaded on 12/8/2025 6:04:23 AM.
This article is licensed under a Creative Commons Attribution-NonCommercial 3.0 Unported Licence.

Table 3 Electrochemical performance evaluation with previously reported MoO_3-based device performance in the literature

Materials	Device configuration (electrolyte)	C_s (F g^{-1}) at I_d (A g^{-1})	E (W h kg^{-1})	P (W kg^{-1})	Cycling stability (%)	Ref.
MoO_3/GF//PANI/(MnO_2-rGO)/PANI	Asymmetric (PVA/KOH gel)	146 (1)	51.91	838	82% (5 A g^{-1}), 5000 cycles	S1
GrMnO_2//GrMoO_3	Asymmetric (1 M Na_2SO_4)	307	42.6	276	—	S2
MoO_3@CNT//MnO_2@CNT	Asymmetric (1 M Na_2SO_4)	61 (0.2)	27.8	524	96.8% (5 A g^{-1}), 10 000 cycles	S3
rGO/MoO_3//rGO/MoO_3	Symmetric (H_2SO_4/PVA gel)	404 (0.5)	14	500	80% (2 A g^{-1}), 5000 cycles	S4
GF-CNTs/MoO_3//GF-CNTs	Asymmetric (1 M KOH)	211.71 (1)	75.27	816.67	94% (8 A g^{-1}), 10 000 cycles	S5
MoO_3/PPy/rGO//MoO_3/PPy/rGO	Symmetric (1 M Na_2SO_4)	99 (0.5)	19.8	301	86% (2 A g^{-1}), 6000 cycles	S6
Ag QDs/MnO_2//Ag QDs/MoO_3	Asymmetric (Na_2SO_4/PVA gel)	119	51.89	22.6	90% 5000 cycles	S8
MoO_3/CDA//EG	Asymmetric (1 M H_2SO_4)	88 (1)	31.3	838.4	86.5% (1 A g^{-1}), 5000 cycles	S9
MoO_3//MoO_3	Symmetric (0.5 M Na_2SO_4)	236 (0.67)	84	1067	76.9% (15 A g^{-1}) 5000 cycles	This work
MoO_3/CdO (3%)//MoO_3/CdO (3%)	Symmetric (0.5 M Na_2SO_4)	348 (0.67)	124	1067	88.9% (15 A g^{-1}) 5000 cycles	This work

calculated from GCD curves at various current densities using eqn (11) and (12), respectively. The results have been demonstrated through a Ragone plot in Fig. 10 and compared with other SCs. The SSC-2 delivered a maximum energy density of 124 W h kg^{-1} at a power density of 1067 W kg^{-1}, surpassing SSC-1, which exhibited a lower energy density of 84 W h kg^{-1} at the same power density. More importantly, the energy density of SSC-2 can still be maintained at 17 W h kg^{-1} as the power density increases to 8000 W kg^{-1}, reflecting an outstanding power capability. The superior efficiency of the SSC-2 highlights the exceptional supercapacitive behavior of the material and outperforms many previously reported MoO_3-based SC devices, as summarized in Table 3. For instance, α-MoO_3 nanorods have been reported to deliver a specific capacitance of 214 F g^{-1} at a current density of 0.1 A g^{-1}, with a cycling stability of only 71.7% retention after 1000 cycles at 1 A g^{-1}.[121] In terms of energy storage, a MoO_3-based supercapacitor achieves an energy density of 24 W h kg^{-1} at a power density of 150 W kg^{-1}, whereas the PPy@MoO_3 nanocomposite offers a lower energy density of 20 W h kg^{-1} at 75 W kg^{-1}.[17] The N-doped Mo_2-C@MoO_3 electrode exhibits a specific capacitance of 322 F g^{-1} at a current density of 0.5 A g^{-1}, while the assembled symmetric supercapacitor delivers an energy density of 37.5 W h kg^{-1} along with a power density of 2.495 W kg^{-1}.[122]

4. Conclusions

An efficient, environmentally friendly, facile hydrothermal approach was utilized to synthesize MoO_3 and MoO_3/CdO binary metal oxides as electrode materials. The 1-D nanobelt architectures of MoO_3 provide short diffusion paths for the movement of electrons and ions, resulting in high capacitance and improved electrochemical performance. With the increase in CdO concentration, there is a corresponding decrease in the size of the nanobelts, leading to a reduction in their aspect ratio. Lower aspect ratio structures generally offer greater resistance to structural failure. The electrochemical performance is assessed using three-electrode configurations through CV, GCD, and EIS. A blend of capacitive and diffusion-controlled mechanisms governs the charge storage process. However, at identical scan rates, the diffusion-controlled contribution predominates over the capacitive contribution, indicating pronounced pseudocapacitive behavior. MoO_3/CdO (3%) exhibits an impressive specific capacitance of 671 F g^{-1} at 0.50 A g^{-1}, higher than other electrodes. The synergistic interaction between the distinctive morphological characteristics and the electrically conductive characteristics of MoO_3 and CdO may cause this enhanced capacitance. The MoO_3/CdO (3%) electrode exhibits a lower intrinsic series and charge transfer resistance, which suggests a faster faradaic response with appreciably lower resistance and contributes to improved capacitive performance. Additionally, the electrode exhibits outstanding cycling stability, retaining nearly 92% of its original capacitance after 5000 cycles. Also, the high coulombic efficiency confirms the enhanced redox reversibility of the electrode material. The SSC-2 exhibited a high energy density of 124 W h kg^{-1} at 1067 W kg^{-1} and maintained a capacitance

 © 2025 The Author(s). Published by the Royal Society of Chemistry

Open Access Article. Published on 22 July 2025. Downloaded on 12/8/2025 6:04:23 AM. This article is licensed under a Creative Commons Attribution-NonCommercial 3.0 Unported Licence.

retention of 88.9% after 5000 cycles at 15 A g^{-1}. These findings suggest that incorporating CdO nanoparticles into MoO_3 nanobelts significantly enhances electrochemical performance, potentially opening the way for new advancements in electrochemical nanodevice fabrication with distinctive properties. Moreover, this study demonstrates that the simple hydrothermal approach can be effectively applied to other transition metal oxides to develop supercapacitor electrode materials.

Data availability

The data will be made available upon request.

Conflicts of interest

There is no conflicts to declare.

Acknowledgements

The authors convey their gratitude to the Department of Physics and the Department of Nanomaterials and Ceramic Engineering, BUET, for their support in the synthesis and characterization of the materials. The authors also acknowledge the Committee for Advanced Studies and Research (CASR), BUET, for financial support. The authors gratefully acknowledge the financial support from the Ministry of Education, Government of Bangladesh, under grant 37.20.0000.004.33.020.23(Part-5).

References

1 A. E. Baumann, D. A. Burns, B. Liu and V. S. Thoi, Metal-organic framework functionalization and design strategies for advanced electrochemical energy storage devices, *Commun. Chem.*, 2019, **2**(1), 1–14, DOI: **10.1038/s42004-019-0184-6**.

2 S. Tanwar, N. Singh and A. L. Sharma, Structural and electrochemical performance of carbon coated molybdenum selenide nanocomposite for supercapacitor applications, *J. Energy Storage*, 2022, **45**, 103797, DOI: **10.1016/j.est.2021.103797**.

3 S. S. H. Zardkhoshoui, A. M. Ameri and B. Davarani, Fabrication of hollow $MnFe_2O_4$ nanocubes assembled by CoS_2 nanosheets for hybrid supercapacitors, *Chem. Eng. J.*, 2022, **435**, 135170, DOI: **10.1016/j.cej.2022.135170**.

4 I. Shaheen, K. S. Ahmad, C. Zequine, R. K. Gupta, A. G. Thomas and M. A. Malik, Modified sol-gel synthesis of Co_3O_4 nanoparticles using organic template for electrochemical energy storage, *Energy*, 2021, **218**, 119502, DOI: **10.1016/j.energy.2020.119502**.

5 J. R. Miller and P. Simon, Materials science: Electrochemical capacitors for energy management, *Science*, 2008, **321**(5889), 651–652, DOI: **10.1126/science.1158736**.

6 M. R. Lukatskaya, B. Dunn and Y. Gogotsi, Multidimensional materials and device architectures for future hybrid energy storage, *Nat. Commun.*, 2016, **7**, 12647, DOI: **10.1038/ncomms12647**.

7 Y. Zhong, X. H. Xia, F. Shi, J. Y. Zhan, J. P. Tu and H. J. Fan, Transition metal carbides and nitrides in energy storage and conversion, *Adv. Sci.*, 2015, **3**(5), 1500286, DOI: **10.1002/advs.201500286**.

8 M. Winter and R. J. Brodd, What are batteries, fuel cells, and supercapacitors?, *Chem. Rev.*, 2004, **104**(10), 4245–4269, DOI: **10.1021/cr020730k**.

9 C. D. Lokhande, D. P. Dubal and O. S. Joo, Metal oxide thin film based supercapacitors, *Curr. Appl. Phys.*, 2011, **11**(3), 255–270, DOI: **10.1016/j.cap.2010.12.001**.

10 P. Simon, Y. Gogotsi and B. Dunn, Where do batteries end and supercapacitors begin?, *Science*, 2014, **343**(6176), 1210–1211, DOI: **10.1126/science.1249625**.

11 S. Ajdari, F. B. Kowsari, E. Shahrak, M. N. Ehsani, A. Kiaei, Z. Torkzaban and H. Ramakrishna, A review on the field patents and recent developments over the application of metal organic frameworks (MOFs) in supercapacitors, *Coord. Chem. Rev.*, 2020, **422**, 213441, DOI: **10.1016/j.ccr.2020.213441**.

12 L. Zhao, X. Sajjad, M. Zheng, Y. Zhao, M. Li, Z. Wu and Z. Qiu, Covalent organic framework templated ordered nanoporous C_{60} as stable energy efficient supercapacitor electrode material, *Carbon*, 2021, **182**, 144–154, DOI: **10.1016/j.carbon.2021.05.061**.

13 R. Barik, A. K. Yadav, S. N. Jha, D. Bhattacharyya and P. P. Ingole, Two-dimensional tungsten oxide/selenium nanocomposite fabricated for flexible supercapacitors with higher operational voltage and their charge storage mechanism, *ACS Appl. Mater. Interfaces*, 2021, **13**(7), 8102–8119, DOI: **10.1021/acsami.0c15818**.

14 C. S. Bongu, M. R. Krishnan, A. Soliman, M. Arsalan and E. H. Alsharaeh, Flexible and Freestanding MoS_2/Graphene Composite for High-Performance Supercapacitors, *ACS Omega*, 2023, **8**(40), 36789–36800, DOI: **10.1021/acsomega.3c03370**.

15 M. Kumar, K. D. Ramachandran, T. Kumar, Y. A. Mohammed and A. A. Kang, Hierarchically fabricated nano flakes-rod-like CoMoO–S supported Ni-foam for high-performance supercapacitor electrode material, *J. Phys. Chem. Solids*, 2024, **185**, 111735, DOI: **10.1016/j.jpcs.2023.111735**.

16 G. Wang, L. Zhang and J. Zhang, A review of electrode materials for electrochemical supercapacitors, *Chem. Soc. Rev.*, 2012, **41**(2), 797–828, DOI: **10.1039/c1cs15060j**.

17 Y. Liu, B. Zhang, Y. Yang, Z. Chang, Z. Wen and Y. Wu, Polypyrrole-coated α-MoO_3 nanobelts with good electrochemical performance as anode materials for aqueous supercapacitors, *J. Mater. Chem. A*, 2013, **1**(43), 13582–13587, DOI: **10.1039/c3ta12902k**.

18 Y. Jiang, J. Liu, J. Peng, S. Qian, D. Luo, D. Wang and Q. Liu, Facile synthesis of α-MoO3 nanobelts and their pseudocapacitive behavior in an aqueous Li2SO4 solution, *J. Mater. Chem. A*, 2013, **1**(7), 2588–2594, DOI: **10.1039/c2ta01120d**.

19 B. Ye, X. Cao, Q. Zhao and J. Wang, Coelectrodeposition of NiSe/ZnSe Hybrid Nanostructures as a Battery-Type Electrode for an Asymmetric Supercapacitor, *J. Phys.*

Open Access Article. Published on 22 July 2025. Downloaded on 12/8/2025 6:04:23 AM. This article is licensed under a Creative Commons Attribution-NonCommercial 3.0 Unported Licence.

Chem. C, 2020, **124**(39), 21242–21249, DOI: 10.1021/acs.jpcc.0c05125.

20 Z. Li, L. Wei, Z. Liu, W. Ding and M. Li, Selenium-doped Se-$CoSe_2$@ ZnSe heterojunction structure derived from ZIF-8 metal organic skeleton is used in high-performance asymmetric supercapacitors, *J. Alloys Compd.*, 2022, **927**, 167100, DOI: 10.1016/j.jallcom.2022.167100.

21 T. Wang, H. C. Chen, F. Yu and X. S. Zhao, Boosting the cycling stability of transition metal compounds-based supercapacitors, *Energy Storage Mater.*, 2019, **16**, 545–573, DOI: 10.1016/j.ensm.2018.09.007.

22 Y. Wang, J. Guo, T. Wang, J. Shao, D. Wang and Y. Yang, Mesoporous Transition Metal Oxides for Supercapacitors, *Nanomaterials*, 2015, **5**(4), 1667–1689, DOI: 10.3390/nano5041667.

23 N. Maheswari and G. Muralidharan, Supercapacitor Behavior of Cerium Oxide Nanoparticles in Neutral Aqueous Electrolytes, *Energy Fuels*, 2015, **29**(12), 8246–8253, DOI: 10.1021/acs.energyfuels.5b02144.

24 C. Rose, A. V Avani, T. S. Xavier, M. Tomy, S. Shaji and E. I. Anila, Symmetric supercapacitor based on Co_3O_4 nanoparticles with an improved specific capacitance and energy density, *J. Energy Storage*, 2024, **80**, 110382, DOI: 10.1016/j.est.2023.110382.

25 J. Chen, J. Xu, S. Zhou, N. Zhao and C. P. Wong, Template-grown graphene/porous Fe_2O_3 nanocomposite: A high-performance anode material for pseudocapacitors, *Nano Energy*, 2015, **15**, 719–728, DOI: 10.1016/j.nanoen.2015.05.021.

26 M. F. Khalid, M. U. Katubi, K. M. Zulfiqar, S. Alrowaili, Z. A. Aadil, M. Al-Buriahi and M. S. Warsi, Boosting the electrochemical activities of MnO_2 for next-generation supercapacitor application: adaptation of multiple approaches, *Fuel*, 2023, **343**, 127946, DOI: 10.1016/j.fuel.2023.127946.

27 M. B. Askari, P. Salarizadeh and M. Hassan, MoO_3/WO_3/rGO as electrode material for supercapacitor and catalyst for methanol and ethanol electrooxidation, *Sci. Rep.*, 2024, 1–11, DOI: 10.1038/s41598-024-59018-2.

28 A. K. Bulla, M. Kumar, V. Devi, R. Kumar, S. Sisodiy, A. K. Dahiya and R. Mishra, Natural resource-derived NiO nanoparticles via aloe vera for high- performance symmetric supercapacitor, *Sci. Rep.*, 2024, **14**(1), 1–11, DOI: 10.1038/s41598-024-57606-w.

29 C. D. Bagde, A. G. Malavekar, D. B. Lokhande, A. C. Khot and S. D. Lokhande, Flexible solid-state asymmetric supercapacitor based on reduced graphene oxide (rGO)/ruthenium oxide (RuO_2) composite electrode, *J. Alloys Compd.*, 2024, **980**, 173591, DOI: 10.1016/j.jallcom.2024.173591.

30 N. B. Rohom, A. B. Londhe, P. U. Han and J. I. Chaure, Conducting polymer wrapped SnO_2/RGO nanocomposite: An efficient high-performance supercapacitor material, *Surf. Interfaces*, 2024, **44**, 103605, DOI: 10.1016/j.surfin.2023.103605.

31 P. Kashyap, T. Bortamuly, R. Elias, L. Das, M. R. Mahanta and D. Saikia, TiO_2–CeO_2/Ag Composite as Electrode Material for Supercapacitors, *ACS Appl. Nano Mater.*, 2024, **7**(5), 4667–4675, DOI: 10.1021/acsanm.3c04601.

32 Y. Jia, D. Zheng, F. Li, Y. Niu, Y. Yang, Y. Mao and X. Yu, V_2O_5 nanosheet arrays/Co_3O_4 nanoneedle arrays composite for supercapacitor with enhanced energy density, *Appl. Surf. Sci.*, 2024, **659**, 159874, DOI: 10.1016/j.apsusc.2024.159874.

33 F. I. Anikpa, P. O. Mee, A. U. Nwanya, A. C. Nkele, A. C. Malavekar, D. B. Osuji and R. U. Ezema, Asymmetric supercapacitor performance of hydrothermally-synthesized MWCNT-WO_3 composite electrode, *J. Energy Storage*, 2024, **81**, 110439, DOI: 10.1016/j.est.2024.110439.

34 S. Sahu, J. Kumar, S. Ahmed, F. Alvi, P. A. Dalela, B. Phase and D. M. Dalela, Electrochemical and electronic structure properties of high-performance supercapacitor based on Nd-doped ZnO nanoparticles, *J. Energy Storage*, 2023, **59**, 106499, DOI: 10.1016/j.est.2022.106499.

35 O. M. Prakash, N. G. Dhananjaya, M. Narayana, A. L. Shaik, D. P. Rosaiah and P. Hussain, High performance one dimensional α-MoO_3 nanorods for supercapacitor applications, *Ceram. Int.*, 2018, **44**(8), 9967–9975, DOI: 10.1016/j.ceramint.2018.03.032.

36 Z. L. Xiao, X. Ding, T. Yuan, L. Shen, Y. Zhong, Q. Zhang and X. Wang, WO_3-x/MoO_{3-x} core/shell nanowires on carbon fabric as an anode for all-solid-state asymmetric supercapacitors, *Adv. Energy Mater.*, 2012, **2**(11), 1328–1332, DOI: 10.1002/aenm.201200380.

37 P. Badica, Preparation through the vapor transport and growth mechanism of the first-order hierarchical structures of MoO_3 belts on sillimanite fibers, *Cryst. Growth Des.*, 2007, **7**(4), 794–801, DOI: 10.1021/cg060893s.

38 S. Kumar, A. Singh, R. Singh, S. Singh, P. Kumar and R. Kumar, Facile h-MoO_3 synthesis for NH_3 gas sensing application at moderate operating temperature, *Sens. Actuators, B*, 2020, **325**, 128974, DOI: 10.1016/j.snb.2020.128974.

39 Q. Sun, M. Wu, G. Jiang, J. Yang, Y. Du, A. Dai and L. Qin, Carbon-anchored molybdenum oxide nanoclusters as efficient catalysts for the electrosynthesis of ammonia and urea, *Angew. Chem.*, 2023, **135**(19), e202301957, DOI: 10.1002/ange.202301957.

40 J. Sun, Y. Meng and B. Zhang, Tribological Behaviors and Lubrication Mechanism of Water-based MoO_3 Nanofluid during Cold Rolling Process, *J. Manuf. Process.*, 2021, **61**, 518–526, DOI: 10.1016/j.jmapro.2020.11.044.

41 Z. Lei, X. Yang, J. Dong and X. Yi, Novel metastable hexagonal MoO_3 nanobelts: Synthesis, photochromic, and electrochromic properties, *Chem. Mater.*, 2009, **21**(23), 5681–5690, DOI: 10.1021/cm9023887.

42 X. D. Hao, L. C. Zhang, M. Ni, M. Liu and J. M. Feng, Simulation of high efficiency silicon heterojunction solar cells with molybdenum oxide carrier selective layer, *Mater. Res. Express*, 2018, **5**(7), 075504, DOI: 10.1088/2053-1591/aace80.

43 Z. L. Mai, L. Q. Hu, B. Chen, W. Qi, Y. Y. Lao, C. S. Yang and R. S. Wang, Lithiated MoO_3 nanobelts with greatly

 © 2025 The Author(s). Published by the Royal Society of Chemistry

Open Access Article. Published on 22 July 2025. Downloaded on 12/8/2025 6:04:23 AM.
This article is licensed under a Creative Commons Attribution-NonCommercial 3.0 Unported Licence.

improved performance for lithium batteries, *Adv. Mater.*, 2007, **19**(21), 3712–3716, DOI: 10.1002/adma.200700883.

44 A. Kumar, A. Sanger, A. Kumar, Y. Kumar and R. Chandra, An efficient α-MnO_2 nanorods forests electrode for electrochemical capacitors with neutral aqueous electrolytes, *Electrochim. Acta*, 2016, **220**, 712–720, DOI: 10.1016/j.electacta.2016.10.168.

45 Y. Zhu, Y. Tan and H. Li, MoO_3 nanoplates preparation via self-sacrifice C_3N_4 for supercapacitors in an acid electrolyte, *J. Energy Storage*, 2023, **60**, 106657, DOI: 10.1016/j.est.2023.106657.

46 I. Shaheen, W. Warsi, M. F. Shahid, M. Khan, M. A. Asghar, M. Ali and Z. Shakir, Carbon Coated MoO_3 Nanowires/Graphene oxide Ternary Nanocomposite for High-Performance Supercapacitors, *Electrochim. Acta*, 2016, **219**, 330–338, DOI: 10.1016/j.electacta.2016.09.069.

47 I. Shakir, M. Shahid, H. W. Yang and D. J. Kang, Structural and electrochemical characterization of α-MoO_3 nanorod-based electrochemical energy storage devices, *Electrochim. Acta*, 2010, **56**(1), 376–380, DOI: 10.1016/j.electacta.2010.09.028.

48 L. Zhou, L. Yang, P. Yuan, J. Zou, Y. Wu and C. Yu, α-MoO_3 Nanobelts : A High Performance Cathode Material for Lithium Ion Batteries, *J. Phys. Chem. C*, 2010, **114**(49), 21868–21872, DOI: 10.1021/jp108778v.

49 N. G. Prakash, M. Dhananjaya, A. L. Narayana and O. M. Hussain, One-dimensional MoO_3/Pd nanocomposite electrodes for high performance supercapacitors, *Mater. Res. Express*, 2019, **6**(8), 085543, DOI: 10.1088/2053-1591/ab273e.

50 H. Wei, X. Jiao, L. Liu, S. Sun, J. Peng, W. Gao and H. Yuan, Synthesis and electrochemical performance of V_2O_5 doped MoO_3 cathode materials, *J. Alloys Compd.*, 2009, **486**(1–2), 672–676, DOI: 10.1016/j.jallcom.2009.07.030.

51 G. D. Park, S. H. Choi and Y. C. Kang, Electrochemical properties of ultrafine TiO_2-doped MoO_3 nanoplates prepared by one-pot flame spray pyrolysis, *RSC Adv.*, 2014, **4**(33), 17382–17386, DOI: 10.1039/c4ra01780c.

52 J. Cao, Y. Cui, Z. Ji, T. Li, W. Xu, K. Zou and R. Hu, Hierarchical MoO_3/MnO_2 core-shell nanostructures with enhanced pseudocapacitive properties, *J. Alloys Compd.*, 2017, **725**, 373–378, DOI: 10.1016/j.jallcom.2017.07.182.

53 S. K. Muduli, S. Pati, S. K. Swain and S. Martha, MoO_3@ZnO nanocomposite as an efficient anode material for supercapacitors: a cost effective synthesis approach, *Energy Fuels*, 2021, **35**(20), 16850–16859, DOI: 10.1021/acs.energyfuels.1c01665.

54 M. I. Pratheepa and M. Lawrence, Synthesis of pure, Cu and Zn doped CdO nanoparticles by co-precipitation method for supercapacitor applications, *Vacuum*, 2019, **162**, 208–213, DOI: 10.1016/j.vacuum.2019.01.042.

55 D. Dhamodharan, K. Yuvakkumar, R. Thirumal, V. Ravi, G. Isacfranklin, M. Alharbi and S. A. Velauthapillai, Effect of Nd^{3+} doping on CdO nanoparticles for supercapacitor applications, *Ceram. Int.*, 2021, **47**(21), 30790–30796, DOI: 10.1016/j.ceramint.2021.07.259.

56 T. A. M. Althubiti, N. A. Hassan, M. M. Waheed, M. S. Aman, S. Khosa, R. Y. Farid and H. M. T. Taha, Fabrication of novel zinc selenide/cadmium oxide nanohybrid electrode via hydrothermal route for energy storage application, *J. Energy Storage*, 2023, **70**, 108154, DOI: 10.1016/j.est.2023.108154.

57 X. Wang, Y. Yang, F. Zhang, J. Tang and Z. Guo, Facile synthesis of Co_3O_4/CdO nanospheres as high rate performance supercapacitors, *Mater. Lett.*, 2020, **261**, 127141, DOI: 10.1016/j.matlet.2019.127141.

58 M. S. Kenesi, A. G. Ghorbani and M. Lashkenari, High electrochemical performance of PANI/CdO nanocomposite based on graphene oxide as a hybrid electrode materials for supercapacitor application, *Int. J. Hydrogen Energy*, 2022, **47**(91), 38849–38861, DOI: 10.1016/j.ijhydene.2022.09.047.

59 A. Anwar, N. Shakoor, A. Ali, G. Ahmad, H. Niaz and N. A. Mahmood, Synthesis and electrochemical characterization of polyaniline doped cadmium oxide (PANI-CdO) nanocomposites for supercapacitor applications,", *J. Energy Storage*, 2022, **55**, 105446, DOI: 10.1016/j.est.2022.105446.

60 H. Sivaram, D. Selvakumar, A. Alsalme, A. Alswieleh and R. Jayavel, Enhanced performance of PbO nanoparticles and PbO-CdO and PbO-ZnO nanocomposites for supercapacitor application, *J. Alloys Compd.*, 2018, **731**, 55–63, DOI: 10.1016/j.jallcom.2017.10.025.

61 R. Sivasamy, P. Venugopal and E. Mosquera, Synthesis of Gd_2O_3/CdO composite by sol-gel method: Structural, morphological, optical, electrochemical and magnetic studies, *Vacuum*, 2020, **175**, 109255, DOI: 10.1016/j.vacuum.2020.109255.

62 B. C. Gupta, M. Chaudhary, P. Singh, A. Verma, A. Yadav and D. Yadav, Development of MoO_3-CdO nanoparticles based sensing device for the detection of harmful acetone levels in our skin and body via nail paint remover, *Sens. Actuators, B*, 2022, **368**, 132102, DOI: 10.1016/j.snb.2022.132102.

63 K. Aloraini, D. A. Al-Baradi and A. M. Kreen, Composition-Dependent Basic Physical Properties and Radiation Shielding Performance of B_2O_3-Li_2O-MoO_3-CdO Glasses, *J. Electron. Mater.*, 2025, **54**, 5928–5935, DOI: 10.1007/s11664-025-11897-5.

64 D. K. Shelke, N. T. Yewale, M. A. Kadam, R. A. Nakate, U. T. Jadhavar and A. A. Shin, Facile hydrothermal synthesis and fabrication of nickel cobalt oxide as an advanced electrode for electrochemical capacitors, *Surf. Interfaces*, 2023, **43**, 103555, DOI: 10.1016/j.surfin.2023.103555.

65 B. H. Park and J. H. Choi, Improvement in the capacitance of a carbon electrode prepared using water-soluble polymer binder for a capacitive deionization application, *Electrochim. Acta*, 2009, **55**(8), 2888–2893, DOI: 10.1016/j.electacta.2009.12.084.

66 B. Pal, S. Yang, S. Ramesh, V. Thangadurai and R. Jose, Electrolyte selection for supercapacitive devices: A critical

Open Access Article. Published on 22 July 2025. Downloaded on 12/8/2025 6:04:23 AM.
This article is licensed under a Creative Commons Attribution-NonCommercial 3.0 Unported Licence.

review, *Nanoscale Adv.*, 2019, **1**(10), 3807–3835, DOI: 10.1039/c9na00374f.

67 F. Ahmad, *et al.*, Recent developments in transition metal oxide-based electrode composites for supercapacitor applications, *J. Energy Storage*, 2024, **81**, 110430, DOI: 10.1016/j.est.2024.110430.

68 S. Zhou, J. Guo, M. Wang, L. Ding, Y. Zhang, Z. Tang and Y. Luo, 1T-MoS_2 nanosheets confined among TiO_2 nanotube arrays for high performance supercapacitor, *Chem. Eng. J.*, 2019, **366**, 163–171, DOI: 10.1016/j.cej.2019.02.079.

69 S. Ullah, E. Shah, M. Z. U. Ahmad, S. A. Sajjad, M. Khan, S. Alzahrani and F. M. Guo, Hydrothermal assisted synthesis of hierarchical SnO_2 micro flowers with CdO nanoparticles based membrane for energy storage applications, *Chemosphere*, 2023, **321**, 138004, DOI: 10.1016/j.chemosphere.2023.138004.

70 J. Nunna, G. P. Siddarapu, H. K. Nimmagadda, V. V. J. Obili, M. H. Ko, T. J. Lim and J. Choi, Biogenic Synthesis of High-Performance α -MoO_3 Nanoparticles from Tryptophan Derivatives for Antimicrobial Agents and Electrode Materials of Supercapacitors, *Int. J. Energy Res.*, 2023, **2023**(1), 6715319, DOI: 10.1155/2023/6715319.

71 S. Sajjad, M. Shah, M. Z. U. Mahmood, F. Javed, M. S. Maryam, R. Ahmad and F. Rahman, CdO nanocubes decorated on rGO sheets as novel high conductivity positive electrode material for hybrid supercapacitor, *J. Alloys Compd.*, 2023, **938**, 168462, DOI: 10.1016/j.jallcom.2022.168462.

72 D. Wang, X. Zhang, Y. Shen and Z. Wu, Ni-doped MoS_2 nanoparticles as highly active hydrogen evolution electrocatalysts, *RSC Adv.*, 2016, **6**(20), 16656–16661, DOI: 10.1039/c6ra02610a.

73 S. G. Nair, J. Satapathy and N. P. Kumar, Influence of synthesis, dopants, and structure on electrical properties of bismuth ferrite ($BiFeO_3$), *Appl. Phys. A:Mater. Sci. Process.*, 2020, **126**(11), 1–14, DOI: 10.1007/s00339-020-04027-x.

74 A. Batoo, K. M. Kumar, G. Yang, Y. Al-Douri, Y. Singh, M. Jotania and R. B. Imran, Structural, morphological and electrical properties of Cd^{2+} doped $MgFe_{2-x}O_4$ ferrite nanoparticles, *J. Alloys Compd.*, 2017, **726**, 179–186, DOI: 10.1016/j.jallcom.2017.07.237.

75 G. Corbel, Y. Laligant, F. Goutenoire, E. Suard and P. Lacorre, Effects of partial substitution of Mo^{6+} by Cr^{6+} and W^{6+} on the crystal structure of the fast oxide-ion conductor structural effects of W^{6+}, *Chem. Mater.*, 2005, **17**(18), 4678–4684, DOI: 10.1021/cm0501214.

76 M. Lübke, J. A. SumbojaLübke, M. Sumboja, A. McCafferty, L. Armer, C. F. Handoko, A. D. Du and Y. Darr, Transition-Metal-Doped α-MnO_2 Nanorods as Bifunctional Catalysts for Efficient Oxygen Reduction and Evolution Reactions, *ChemistrySelect*, 2018, **3**(9), 2613–2622, DOI: 10.1002/slct.201702514.

77 L. Zhang, X. Song, X. Gao, S. Xu, Y. Cheng, X. Zhao and H. Huo, Facile synthesis of yolk-shell MoO_2 microspheres with excellent electrochemical performance as a Li-ion battery anode, *J. Mater. Chem. A*, 2013, **1**(23), 6858–6864, DOI: 10.1039/c3ta10399d.

78 M. R. Islam, M. A. Bhuiyan, M. H. Ahmed and M. Rahaman, Hydrothermal synthesis of NiO nanoparticles decorated hierarchical MnO_2 nanowire for supercapacitor electrode with improved electrochemical performance, *Heliyon*, 2024, **10**(4), e26631, DOI: 10.1016/j.heliyon.2024.e26631.

79 S. R. Rajiv Chandar, N. Agilan, S. Thangarasu, R. Muthukumarasamy, N. Chandrasekaran, J. Arunachalam and S. Akshaya, Elucidation of efficient dual performance in photodegradation and antibacterial activity by a promising candidate Ni-doped MoO_3 nanostructure, *J. Sol-Gel Sci. Technol.*, 2021, **100**(3), 451–465, DOI: 10.1007/s10971-020-05382-0.

80 M. Kawsar, M. S. Hossain, N. M. Bahadur and S. Ahmed, Synthesis of nano-crystallite hydroxyapatites in different media and a comparative study for estimation of crystallite size using Scherrer method, Halder-Wagner method size-strain plot, and Williamson-Hall model, *Heliyon*, 2024, **10**(3), e25347, DOI: 10.1016/j.heliyon.2024.e25347.

81 R. Robert and P. Novák, Structural Changes and Microstrain Generated on $LiNi_{0.80}Co_{0.15}Al_{0.05}O_2$ during Cycling: Effects on the Electrochemical Performance, *J. Electrochem. Soc.*, 2015, **162**(9), A1823–A1828, DOI: 10.1149/2.0721509jes.

82 L. Ma, L. Xu, X. Xu, X. Zhou, J. Luo and L. Zhang, Cobalt-doped edge-rich MoS_2/nitrogenated graphene composite as an electrocatalyst for hydrogen evolution reaction, *Mater. Sci. Eng., B*, 2016, **212**, 30–38, DOI: 10.1016/j.mseb.2016.07.014.

83 A. Rabbani and S. Salehi, Dynamic modeling of the formation damage and mud cake deposition using filtration theories coupled with SEM image processing, *J. Nat. Gas Sci. Eng.*, 2017, **42**, 157–168, DOI: 10.1016/j.jngse.2017.02.047.

84 X. Yang, C. Cheng, Y. Wang, L. Qiu and D. Li, Liquid-mediated dense integration of graphene materials for compact capacitive energy storage, *Science*, 2013, **341**(6145), 534–537, DOI: 10.1126/science.1239089.

85 F. Zhou, J. Lian, J. Hou, L. Zhang, J. Gou, H. Xia and M. Gao, Ultrahigh volumetric capacitance and cyclic stability of fluorine and nitrogen co-doped carbon microspheres, *Nat. Commun.*, 2015, **6**, 8503, DOI: 10.1038/ncomms9503.

86 J. Yang, J. Xiao, X. Chen, P. Zhu, K. Cheng, K. Ye and K. Yan, Creating oxygen-vacancies in MoO_{3-x} nanobelts toward high volumetric energy-density asymmetric supercapacitors with long lifespan, *Nano Energy*, 2019, **58**, 455–465, DOI: 10.1016/j.nanoen.2019.01.071.

87 B. A. Ali, O. I. Metwalli, A. S. G. Khalil and N. K. Allam, Unveiling the Effect of the Structure of Carbon Material on the Charge Storage Mechanism in MoS_2-Based Supercapacitors, *ACS Omega*, 2018, **3**(11), 16301–16308, DOI: 10.1021/acsomega.8b02261.

88 S. J. Patil, B. H. Patil, R. N. Bulakhe and C. D. Lokhande, Electrochemical performance of a portable asymmetric supercapacitor device based on cinnamon-like La_2Te_3

 © 2025 The Author(s). Published by the Royal Society of Chemistry

Open Access Article. Published on 22 July 2025. Downloaded on 12/8/2025 6:04:23 AM. This article is licensed under a Creative Commons Attribution-NonCommercial 3.0 Unported Licence.

prepared by a chemical synthesis route, *RSC Adv.*, 2014, **4**(99), 56332–56341, DOI: 10.1039/c4ra09124h.

89 X. Zhao, N. Fan, H. Zhang, M. Ma, J. Du, Z. Yan and B. Jiang, Simple electrodeposition of MoO_3 film on carbon cloth for high-performance aqueous symmetric supercapacitors, *Chem. Eng. J.*, 2020, **390**, 124477, DOI: 10.1016/j.cej.2020.124477.

90 F. Wu, Q. He, T. Zhang, Y. Zhang, J. Wang, Z. Liu and Y. Ran, Cyclic stability of supercapacitors: materials, energy storage mechanism, test methods, and device, *J. Mater. Chem. A*, 2021, **9**(43), 24094–24147, DOI: 10.1039/d1ta06815f.

91 Z. M. Riyas, C. Priya, R. Premila, G. Maheshwaran, S. Sudhahar and M. R. Prabhu, Synergistic effect of La_2O_3-Nio nanocomposite based electrode for electrochemical high-performance asymmetric supercapacitor applications, *J. Energy Storage*, 2022, **53**, 104988, DOI: 10.1016/j.est.2022.104988.

92 I. Shaheen, K. S. Ahmad, C. Zequine, R. K. Gupta, A. G. Thomas and M. A. Malik, Electrochemical energy storage by nanosized MoO_3/PdO material: Investigation of its structural, optical and electrochemical properties for supercapacitor, *J. Energy Storage*, 2021, **36**, 102447, DOI: 10.1016/j.est.2021.102447.

93 R. S. Ji, J. Zhang, L. L. Ji, H. Li, Y. Zhao, X. Bai and X. Ruoff, Nanoporous $Ni(OH)_2$ thin film on 3d ultrathin-graphite foam for asymmetric supercapacitor, *ACS Nano*, 2013, **7**(7), 6237–6243, DOI: 10.1021/nn4021955.

94 C. Wang, Y. Liu, Y. Sun, L. Cui and J. Liu, 3D nanoflower-like and core-shell structured MCo_2O_4@MCo_2S_4@polypyrrole (M = Cu, Mn) composites as supercapacitor electrode materials with ultrahigh specific capacitances, *J. Mater. Chem. A*, 2023, **11**(14), 7639–7651, DOI: 10.1039/d2ta09578e.

95 Y. Han, C. Zhang, K. J. Chen and T. Wang, 2D metal-organic framework derived ultra-thin nitrogen-doped oxygen rich porous carbon nanosheets for zinc-ion hybrid supercapacitors, *J. Mater. Chem. A*, 2024, **12**, 24296–24307, DOI: 10.1039/d4ta03899a.

96 X. Chen, Z. Ding, H. Yu, H. Ge, W. Liu and S. Sun, Facile fabrication of $CuCo_2S_4$ nanoparticles/MXene composite as anode for high-performance asymmetric supercapacitor, *Mater. Chem. Front.*, 2021, **5**(20), 7606–7616, DOI: 10.1039/d1qm01029h.

97 L. Rani and J. I. Han, Unraveling the electrochemical properties of $CuCo_2S_4$ nanoflakes adorned on multi-walled carbon nanotubes for high-performing aqueous asymmetric supercapacitor, *J. Energy Storage*, 2024, **97**, 112749, DOI: 10.1016/j.est.2024.112749.

98 A. Lakshmi-Narayana, N. Attarzadeh, V. Shutthanandan and C. V. Ramana, High-Performance $NiCo_2O_4$/Graphene Quantum Dots for Asymmetric and Symmetric Supercapacitors with Enhanced Energy Efficiency, *Adv. Funct. Mater.*, 2024, 2316379, DOI: 10.1002/adfm.202316379.

99 I. Naskar, P. Ghosal and M. Deepa, Efficient charge storage by $ZnCo_2S_4$ nanoflakes@$MgCo_2O_4$ nanorods composite in Mg^{2+}/Zn^{2+}/K^+ conducting electrolytes, *J. Energy Storage*, 2022, **55**, 105389, DOI: 10.1016/j.est.2022.105389.

100 J. L. Zhang, A. Ran, P. Han, X. Ke, S. Qiu, A. Zhang and Z. Zuo, Donor-π-acceptor heterojunctions constructed from the rGO network and redox-active covalent organic frameworks for high-performance supercapacitors, *J. Mater. Chem. A*, 2024, **12**(33), 22037–22044, DOI: 10.1039/d4ta03481c.

101 L. E. Helseth, Comparison of methods for finding the capacitance of a supercapacitor, *J. Energy Storage*, 2021, **35**, 102304, DOI: 10.1016/j.est.2021.102304.

102 R. K. Alkhalaf, S. Ranaweera, C. K. Kahol, P. K. Siam, K. Adhikari, H. Mishra and S. R. Gupta, Electrochemical energy storage performance of electrospun $CoMn_2O_4$ nanofibers, *J. Alloys Compd.*, 2017, **692**, 59–66, DOI: 10.1016/j.jallcom.2016.09.005.

103 K. Sarkar, D. Khan, G. G. Singh and A. K. Mandal, High-performance pseudocapacitor electrodes based on α-Fe_2O_3/MnO_2 core–shell nanowire heterostructure arrays, *J. Phys. Chem. C*, 2013, **117**(30), 15523–15531.

104 M. Rahaman, M. J. Islam, A. Ul-Hamid and M. R. Islam, Role of defects on the electrochemical performance of MnS nanoparticles decorated 2H-MoS_2 nanoflower: Experimental and theoretical investigation, *Surf. Interfaces*, 2024, **45**, 103886, DOI: 10.1016/j.surfin.2024.103886.

105 M. A. Siddiki, M. R. Abtahee, S. A. Rahaman, M. Islam and M. R. Zubair, Disorder induced augmentation of the specific capacitance of δ-MnO_2 nanoflowers by incorporating Fe_3O_4 nanodiamonds for supercapacitor electrodes, *Mater. Adv.*, 2024, **5**(24), 9641–9655, DOI: 10.1039/d4ma00880d.

106 M. De la Fuente Salas, I. M. Sudhakar and Y. N. Selvakumar, Synthesis of amorphous $NiCo_zV_xO_y$ nanosphere as a positive electrode materials via a facile route for asymmetric supercapacitors, *J. Power Sources*, 2021, **492**, 229623, DOI: 10.1016/j.jpowsour.2021.229623.

107 I. M. De La Fuente Salas, Y. N. Sudhakar and M. Selvakumar, High performance of symmetrical supercapacitor based on multilayer films of graphene oxide/polypyrrole electrodes, *Appl. Surf. Sci.*, 2014, **296**, 195–203, DOI: 10.1016/j.apsusc.2014.01.080.

108 S. Hasan, A. H. Reaz, S. Das, C. K. Roy and M. A. Basith, $CuCo_2S_4$-MoS_2 nanocomposite: a novel electrode for high-performance supercapacitors, *J. Mater. Chem. C*, 2022, **10**(20), 7980–7996, DOI: 10.1039/d2tc01026g.

109 S. M. Gateman, O. Gharbi, H. Gomes de Melo, K. Ngo, M. Turmine and V. Vivier, On the use of a constant phase element (CPE) in electrochemistry, *Curr. Opin. Electrochem.*, 2022, **36**, 1–14, DOI: 10.1016/j.coelec.2022.101133.

110 X. Zhu, L. Shen, F. Smith Jr and R. L. Qi, High-performance supercapacitor electrode materials from chitosan via hydrothermal carbonization and potassium hydroxide activation, *Energy Technol.*, 2017, **5**(3), 452–460, DOI: 10.1002/ente.201600337.

Open Access Article. Published on 22 July 2025. Downloaded on 12/8/2025 6:04:23 AM.
This article is licensed under a Creative Commons Attribution-NonCommercial 3.0 Unported Licence.

111 M. Sakthivel, R. Sukanya, S. M. Chen, K. Pandi and K. C. Ho, Synthesis and characterization of bimetallic nickel-cobalt chalcogenides ($NiCoSe_2$, $NiCo_2S_4$, and $NiCo_2O_4$) for non-enzymatic hydrogen peroxide sensor and energy storage: Electrochemical properties dependence on the metal-to-chalcogen composition, *Renewable Energy*, 2019, **138**, 139–151, DOI: 10.1016/j.renene.2019.01.079.

112 Rusi and S. R. Majid, Effects of electrodeposition mode and deposition cycle on the electrochemical performance of MnO_2-NiO composite electrodes for high-energy-density supercapacitors, *PLoS One*, 2016, **11**(5), 1–16, DOI: 10.1371/journal.pone.0154566.

113 R. Dubal, D. P. Gund, G. S. Lokhande and C. D. Holze, Controlled Growth of CoS_x Nanostrip Arrays (CoS_x-NSA) on Nickel Foam for Asymmetric Supercapacitors, *Energy Technol.*, 2014, **2**(4), 401–408, DOI: 10.1002/ente.201300193.

114 G. Xiong, K. P. S. S. Hembram, R. G. Reifenberger and T. S. Fisher, MnO_2-coated graphitic petals for supercapacitor electrodes, *J. Power Sources*, 2013, **227**, 254–259, DOI: 10.1016/j.jpowsour.2012.11.040.

115 R. Farzana, K. Hassan and V. Sahajwalla, Manganese oxide synthesized from spent Zn-C battery for supercapacitor electrode application, *Sci. Rep.*, 2019, **9**(1), 1–12, DOI: 10.1038/s41598-019-44778-z.

116 M. Majumder, R. B. Choudhary, A. K. Thakur and I. Karbhal, Impact of rare-earth metal oxide (Eu_2O_3) on the electrochemical properties of a polypyrrole/CuO polymeric composite for supercapacitor applications, *RSC Adv.*, 2017, 7(32), 20037–20048, DOI: 10.1039/c7ra01438d.

117 K. C. Veerakumar, P. Sangili, A. Manavalan, S. Thanasekaran and P. Lin, Research Progress on Porous Carbon Supported Metal/Metal Oxide Nanomaterials for Supercapacitor Electrode Applications, *Ind. Eng. Chem. Res.*, 2020, **59**(14), 6347–6374, DOI: 10.1021/acs.iecr.9b06010.

118 S. K. Pati, D. Patra, S. Muduli, S. Mishra and S. Park, Conjugated polymer electrodes fabricated using rylene-based acceptors toward high energy and power density symmetric supercapacitors operable in an organic electrolyte environment, *J. Mater. Chem. A*, 2024, **12**(32), 21165–21175, DOI: 10.1039/d4ta03711a.

119 J. Sun, H. Zong, H. Huang, W. Duan, L. Dong, J. Sun and Y. Liu, A Flexible Asymmetric Supercapacitor Assembled by Dahlia-Like Core-Shell Cobalt/Tin-Based Chalcogenide@Nickel Hydroxide Grown on Reduced Graphene Oxide, *J. Mater. Chem. A*, 2024, **12**(40), 27381–27392, DOI: 10.1039/d4ta01936a.

120 C. V. Lakshmi-Narayana, A. Attarzadeh, N. Shutthanandan and V. Ramana, High-Performance $NiCo_2O_4$/Graphene Quantum Dots for Asymmetric and Symmetric Supercapacitors with Enhanced Energy Efficiency, *Adv. Funct. Mater.*, 2024, **34**, 2316379, DOI: 10.1002/adfm.202316379.

121 Z. Cui, W. Yuan and C. M. Li, Template-mediated growth of microsphere, microbelt and nanorod α-MoO_3 structures and their high pseudo-capacitances, *J. Mater. Chem. A*, 2013, **1**(41), 12926–12931, DOI: 10.1039/c3ta12688a.

122 A. Cevik, E. Gunday, S. T. Iqbal, A. Akhtar and S. Bozkurt, Synthesis of hierarchical multilayer N-doped Mo_2C@MoO_3 nanostructure for high-performance supercapacitor application, *J. Energy Storage*, 2022, **46**, 103824, DOI: 10.1016/j.est.2021.103824.

 © 2025 The Author(s). Published by the Royal Society of Chemistry